Interannual Variability of OLR as Observed by AIRS and CERES

Joel Susskind, NASA Goddard Space Flight Center[1]
Gyula Molnar, Morgan State University/GESTAR[2]
Lena Iredell, Science Applications International Corporation[3]
Norman G. Loeb, NASA Langley Research Center[4]

[1]J. Susskind, NASA GSFC, Code 610, Greenbelt, MD 20771, Joel.Susskind@nasa.gov
[2]G. Molnar, MSU/GESTAR, NASA GSFC, Code 610, Greenbelt, MD 20771, Gyula.I.Molnar@nasa.gov
[3]L. Iredell, SAIC, NASA GSFC, Code 610, Greenbelt, MD 20771, Lena.Iredell@nasa.gov
[4]N. Loeb, NASA LARC, Mail Stop 420, Hampton, VA 23681, Norman.G.Loeb@nasa.gov

Abstract

The paper examines spatial anomaly time series of Outgoing Longwave Radiation (OLR) and Clear Sky OLR (OLR_{CLR}) as determined using observations from CERES Terra and AIRS over the time period September 2002 through June 2011. We find excellent agreement of the two OLR data sets in almost every detail down to the 1° x 1° spatial grid point level. The extremely close agreement of OLR anomaly time series derived from observations by two different instruments implies high stability of both sets of results. Anomalies of global mean, and especially tropical mean, OLR are shown to be strongly correlated with an El Niño Index. These correlations explain that the recent global and tropical mean decreases in OLR over the time period studied are primarily the result of a transition from an El Niño condition at the beginning of the data record to La Niña conditions toward the end of the data period. We show that the close correlation of mean OLR anomalies with the El Niño Index can be well accounted for by temporal changes of OLR within two spatial regions, one to the east of, and one to the west of, the NOAA Niño-4 region. Anomalies of OLR in these two spatial regions are both strongly correlated with the El Niño Index as a result of the strong anti-correlation of anomalies of cloud cover and mid-tropospheric water vapor in these two regions with the El Niño Index.

1. Introduction

Outgoing Longwave Radiation (OLR) is a critical component of the Earth's radiation budget and represents the total radiation going to space emitted by the earth-atmosphere system and integrated over all angles. OLR products have been generated and monitored globally since 1975 based on broad spectral band measurements taken at a given satellite zenith angle by the Earth Radiation Balance (ERB) instrument on the Nimbus-6 and Nimbus-7 satellites [*Jacobowitz et al.,* 1984; *Kyle et al.,* 1993]; the Earth Radiation Budget Experiment (ERBE) instrument on

NOAA-9, NOAA-10, and Earth Radiation Budget Satellite (ERBS) [*Barkstrom*, 1989]; the Advanced Very High Resolution Radiometer (AVHRR) instrument on NOAA operational satellites [*Gruber et al.,* 1994, and references therein]; and most recently by Clouds and Earth's Radiant Energy System (CERES), which has flown on EOS Terra since 2000 and on EOS Aqua since 2002 [*Wielicki et al*., 1996]. Multiyear OLR data sets have also been generated via radiative transfer calculations, which compute OLR for a given scene using surface, atmospheric, and cloud products for that scene derived from the atmospheric sounders Television and Infrared Observation Satellite (TIROS) Operational Vertical Sounder (TOVS) [*Susskind et al.*, 1993] and Atmospheric Infrared Sounder (AIRS) [*Susskind et al*., 2011].

OLR has been widely used as a proxy for tropical convective activity and rainfall, particularly in diagnosing and understanding tropical intraseasonal to interannual variability and monsoons [*Kidson et al*., 2002; *Jones et al*., 2004; *Barlow et al*., 2005; *Kiladis et al*., 2005; *Hoyos and Webster*, 2007; *Wong et al*., 2008; *Chiodi and Harrison*, 2010; *Loeb et al*., 2012a]. In addition, OLR has been used in studies of earth's radiation balance [*Clement and Soden*, 2005; *Fasullo and Trenberth*, 2008] and atmospheric model validation [*Allan et al*., 2003]. More importantly, anomalies and trends of OLR have been used to study climate feedbacks and processes [*Chu and Wang*, 1997; *Soden and Held,* 2006; *Soden et al*., 2008; *Dessler et al*., 2008; *Huang and Ramaswamy*, 2009; *Chung et al*., 2010; *Dessler,* 2010; *Trenberth et al*., 2010; *Zelinka and Hartmann,* 2011; *Zelinka et al*., 2012a, 2012b; *Vander Haar et al*., 2012]. *Dessler* [2010] has estimated the magnitude of the cloud feedback in response to short-term climate variations by analyzing the top-of-atmosphere radiation budget and surface temperature variations from March 2000 to February 2010, and has found that as the surface warms, cloud changes lead to trapping additional energy, i.e., the longwave cloud feedback is positive. He has

93 also shown that El Niño/La Niña variability is the primary source of climate variations during
94 this period. *Vander Haar et al.* [2012] showed that El Niño/La Niña variability also influences
95 global mean total precipitable water, with larger values occurring during El Niño periods.
96 *Zelinka and Hartmann* [2011] investigated the response of tropical mean cloud parameters to the
97 ENSO cycle and their effect on top of atmosphere radiative fluxes. They found that the tropical
98 mean fractional high cloud cover decreases during El Niño periods, which would tend to raise
99 OLR, while the height of these clouds increases, which would tend to lower OLR. From the
100 radiative perspective, changes in the high cloud fractional cloud cover dominated those of the
101 cloud height, and tropical mean OLR consequently increases during El Niño periods. *Zelinka*
102 *and Hartmann* [2011] also validated AIRS water vapor amounts with Microwave Limb Sounder
103 (MLS) measurements for pressures greater than 150 mb. This is significant since we use AIRS-
104 derived 500 mb specific humidity in this study.

105 This paper has two main objectives. The first objective is to compare anomaly time-series
106 of CERES and AIRS OLR products, generated by the CERES and AIRS Science Teams
107 respectively, over the eight year 10 month overlap period of the two data sets, September 2002
108 through June 2011. This comparison shows excellent agreement of these anomaly time series
109 down to the 1˚ x 1˚ spatial scale. Behavior of OLR over this short time period should not be
110 taken in any way as being indicative of what long term trends might be. The ability to begin to
111 draw potential conclusions as to whether there are long term drifts with regard to the earth's
112 OLR, beyond the effects of normal interannual variability, would require consistent calibrated
113 global observations for a time period of at least 20 years, if not longer. Nevertheless, a very close
114 agreement of the eight year 10 month OLR anomaly time series derived using two different
115 instruments in two very different manners is an encouraging result. It demonstrates that one can

have confidence in the 1˚ x 1˚ OLR anomaly time series as observed by each instrument over the same time period. The second objective of the paper is to explain why recent values of global mean, and especially tropical mean, OLR have been strongly correlated with El Niño/La Niña variability and why both have decreased over the time period under study.

2. AIRS and CERES OLR data sets used

In this paper we use the operational monthly mean OLR and OLR_{CLR} data products produced by the AIRS and CERES Science Teams. We obtained the AIRS OLR products from the Goddard Earth Sciences (GES) Data and Information Services Center (DISC) and the CERES products from the CERES Science Team website.

AIRS was launched on the EOS Aqua satellite in a 1:30 AM/PM local crossing time orbit in May 2002. The operational processing of AIRS data began after AIRS became stable in September 2002. We use the AIRS Version-5 monthly mean Level-3 1˚ x 1˚ latitude-longitude grid products which contain separate products generated for each of the 1:30 AM and PM local time orbits. We averaged the AM and PM products together to generate and use a single monthly mean product on the 1˚ x 1˚ grid for each month. In addition to AIRS OLR and OLR_{CLR}, we also use the AIRS Level-3 surface skin temperatures, water vapor profiles, and cloud products to demonstrate the behavior of factors contributing significantly to the anomaly time series of OLR. Section 3 provides a discussion of how the AIRS Science Team OLR and OLR_{CLR} products were computed at the GES DISC.

CERES has flown on both EOS Terra, which was launched in December 1999 on a 10:30 AM/PM local crossing time orbit, and on EOS Aqua, the same platform that carries AIRS. The CERES Science Team generates a number of different OLR data sets using CERES observations. The latest versions of the longest record CERES OLR data sets are referred to as

139 the CERES Energy Balanced And Filled (EBAF) Edition-2.6r data sets, which like AIRS, are
140 Level-3 products presented on a 1˚ x 1˚ latitude-longitude grid. The CERES EBAF data set was
141 obtained from http://ceres.larc.nasa/gov/order_data.php. CERES EBAF Edition-2.6r uses the
142 latest calibration improvements with Edition-2 CERES cloud retrievals [*Minnis et al*., 2008,
143 2011], angular dependence models [*Loeb et al*., 2005], and time-space averaging [*Doelling et al*.,
144 2012]. At the time of this writing, the Level-3 CERES Terra EBAF Edition-2.6r OLR data set
145 extended to June 2011 and the AIRS Level-3 products extended to August 2012. There was no
146 comparable EBAF Edition-2.6 data set available for CERES Aqua. For these reasons, the
147 comparisons shown in this paper use CERES Terra and AIRS OLR products for the overlap time
148 period September 2002 through June 2011.

149 3. Computation of AIRS OLR as a function of surface and atmospheric conditions

150 OLR at a given location is affected primarily by the earth's skin surface temperature, T_s;
151 skin surface spectral emissivity, ε_v; atmospheric vertical temperature profile, *T(p)* and water
152 vapor profile, *q(p);* as well as the heights, amounts, and spectral emissivities of multiple layers of
153 cloud cover. OLR also depends on the vertical distributions of trace gases such as $O_3(p)$, $CH_4(p)$,
154 $CO_2(p)$, and *CO(p).* AIRS surface and atmospheric products are derived for each AIRS Field of
155 Regard (FOR), which is comprised of the 3x3 array of AIRS Fields of View (FOVs) lying within
156 a single 45 km Advanced Microwave Sounding Unit (AMSU)-A footprint. OLR can be
157 computed for each FOR, given all the needed geophysical parameters, using an OLR Radiative
158 Transfer Algorithm (RTA). Mehta and Susskind developed such an OLR RTA for use in
159 conjunction with the TOVS retrieved products [*Susskind et al*., 1997] in order to generate the
160 TOVS Pathfinder Path-A OLR data set [*Mehta and Susskind,* 1999a, 1999b]. AIRS OLR has

been computed using AIRS/AMSU sounding products in a completely analogous manner, including use of the same Mehta and Susskind OLR RTA [*Susskind et al*., 2003].

AIRS measures Infrared (IR) channel radiances over the interval 650 cm^{-1} to 2668 cm^{-1}. Most AIRS OLR products shown in this paper were derived using the AIRS Science Team Version-5 retrieval algorithm [*Susskind et al*., 2011] which generates the values of T_s, ε_v, $T(p)$, $q(p)$, $O_3(p)$, and cloud parameters from which OLR and OLR_{CLR} are computed. The AIRS Version-5 OLR product, referred to as F below, is computed as a sum of fluxes in 14 contiguous spectral bands according to

$$F = \sum_{j=1}^{14} F_j = \sum_{j-1}^{14} \left[(1 - \alpha\varepsilon_{1j} - \alpha\varepsilon_{2j}) F_{j,CLR} + \alpha\varepsilon_{1j} F_{j,CLD1} + \alpha\varepsilon_{2j} F_{j,CLD2} \right] \quad (1)$$

where $F_{j,CLR}$ is the computed clear sky flux going to space integrated over all angles emanating from spectral band j; $F_{j,CLDk}$ is the analogous computed flux emanating from an opaque cloud at cloud top pressure p_k; and $\alpha\varepsilon_{kj}$ is the radiatively effective cloud fraction for the cloud at pressure p_k, which is given by the product of the geometric fractional cloud cover α_k as seen from above and the emissivity of that cloud in spectral band j.

Mehta and Susskind [1999a,1999b] compute $F_{j,CLR}$ according to

$$F_{j,CLR} = \Pi \left[\varepsilon_j B(\nu_j, T_s) \tau_j(p_s) + \int_{\ln p_s}^{\ln \bar{p}} B(\nu_j, T(p)) \frac{d\tau_j(p)}{d \ln p} d \ln p \right] \quad (2)$$

where $B(\nu, T)$ is the Planck Blackbody function evaluated at frequency ν and temperature T, ν_j is the central frequency of spectral band j, ε_j is the surface emissivity in band j, and the term $\tau_j(p)$ represents the effective band averaged atmospheric transmittance in band j from pressure p to the top of the atmosphere $\bar{p}$. Mehta and Susskind parameterize $\tau_j(p)$ as a

function of temperature, moisture, and ozone profile. To first order, the integral in Equation 2 can be approximated by $B(\nu_j, T(p_j))$ x $(1-\tau_j(p_s))$ where p_j is a band effective pressure for which $\tau_j(p_j) = e^{-1}$. $F_{j,CLD}$ is computed in an analogous way to $F_{j,CLR}$, but T_s is replaced by $T(p_k)$ and p_s is replaced by p_k in Equation 2. According to Equations 1 and 2, everything else being held constant, *F* increases with increasing temperature, which increases both the surface and atmospheric contributions in Equation 2. *F* also decreases with increasing atmospheric water vapor, which decreases $\tau_j(p)$, and consequently decreases the band effective pressure p_j in bands sensitive to water vapor absorption, especially for very moist (tropical) cases. In addition, *F* decreases with increasing $\alpha\varepsilon$, especially for high (cold) clouds.

The band transmittance parameterization coefficients used by Mehta and Susskind are computed based on line-by-line calculations [*Susskind and Searl*, 1978] which used the atmospheric line parameter data base of *McClatchey et al*. [1972]. The spectral bands used in Equation 1 range from 2 cm^{-1} through 2750 cm^{-1}. There is no need to make radiometric measurements at all frequencies in order to perform the calculations shown in Equations 1 and 2. The AIRS Version-5 retrieval algorithm determines the surface spectral emissivity ε_v as a function of frequency over the AIRS spectral range using AIRS observations. Surface emissivities at frequencies lower than 650 cm^{-1}, which are not observed by AIRS, are set equal to those at 650 cm^{-1} and are irrelevant with regard to the computation of OLR in any event because the atmosphere is opaque at those frequencies. The AIRS Version-5 retrieval algorithm determines the effective cloud fraction $\alpha\varepsilon_{kj}$ at 800 cm^{-1} for each of up to two cloud layers *k.* The clouds are assumed to be gray, that is, $\alpha\varepsilon_{kj}$ is assumed to be independent of frequency in the calculation of OLR. This is a valid approximation for opaque clouds but not so for cirrus clouds

which have a cloud spectral emissivity that depends on the cloud drop size distribution. The results shown later in this paper demonstrate that the gray cloud approximation does not appear to have significant negative consequences with regard to the study of OLR anomaly time-series. No other approximations are made in the calculation of Equation 1.

AIRS OLR_{CLR} is also a product computed for each AIRS FOR obtained by setting both $\alpha\varepsilon_1$ and $\alpha\varepsilon_2$ equal to zero in Equation 1. Geophysical parameters are determined from AIRS observations under both cloud-free and cloudy conditions, though their quality is poorer under very cloudy conditions, especially at or near the surface. For this reason, the AIRS Version-5 OLR_{CLR} product for a given FOR is included in the generation of the Level-3 monthly mean gridded OLR_{CLR} product only for those cases in which the AIRS retrieved cloud fraction is less than 90% and which also pass an additional OLR_{CLR} quality control procedure which indicates the retrieval is of acceptable accuracy down to the surface [*Susskind et al*., 2011]. Quality Controlled AIRS Version-5 OLR_{CLR} products that are included in the generation of the OLR_{CLR} Level-3 product are produced in roughly 75% of the FOR's observed by AIRS. The OLR product generated for each FOR is always included in the Level-3 OLR product, both because of the need for complete sampling with regard to OLR, and also because computed values of OLR are not affected significantly by surface and atmospheric conditions beneath the cloud in very cloudy cases.

The CERES Science Team uses a different procedure for determining the ensemble of cases to be included in its Level-3 OLR_{CLR} product. The gridded CERES OLR_{CLR} product is generating by averaging values of CERES OLR only for those CERES footprints determined to be cloud-free by use of coincident Moderate Resolution Imaging Spectroradiometer (MODIS) spectral radiance measurements. The MODIS cloud mask used by the CERES Science Team is

described in *Minnis et al*. [2011]. As a result of this difference in sampling methodologies, the AIRS monthly mean OLR_{CLR} product includes a significantly larger ensemble of cases than that found in the CERES monthly mean OLR_{CLR} product. The significant sampling differences between the two ensembles of cases included in each OLR_{CLR} data set is most likely the largest factor that would negatively impact the comparison of OLR_{CLR} anomaly time series contained in the AIRS and CERES Level-3 data sets.

This paper also shows some results comparing OLR computed using the prototype AIRS Version-6 Science Team retrieval algorithm with the Version-5 OLR product. AIRS Version-6 uses an improved OLR RTA [*Iacono et al*., 2008] in the computation of OLR. The approach used to compute OLR in Version-6 is very similar to that used in Version-5, with the minor difference that 16 spectral bands are used in the Version-6 OLR RTA as opposed to the 14 bands used in Equation 1. This new OLR RTA also has two very important upgrades compared to *Mehta and Susskind* [1999a, 1999b]. Most significantly, the new OLR RTA is generated using more up to date line absorption parameters, especially in the very strong water vapor absorption band near 300 cm^{-1}. In addition, the new OLR RTA allows for inclusion of the effects of variations in space and time of CO_2 profiles, as well as those of other minor absorption species such as CO, CH_4, and N_2O, in the calculation of OLR, which were not included in the Version-5 OLR RTA. The AIRS Version-6 retrieval algorithm also has other improvements in methodology which lead to improved values of the geophysical parameters themselves [*Susskind et al*., 2012]. As of the writing of this paper, the AIRS Science Team Version-6 retrieval algorithm has been finalized and will become operational at the Goddard DISC in late 2012. The AIRS Version-6 retrieval algorithm has been tested at the AIRS Science Team Computing

248 Facility (ASTCF) at JPL for the months of January, April, August, and October for each of 2003,
249 2007, and 2011. We show some of the OLR related results of these tests later in the paper.

250 4. Comparison of AIRS and CERES OLR and OLR_{CLR} Data Records

251 Figure 1a shows global mean monthly mean values of AIRS Version-5 OLR and
252 OLR_{CLR}, as well as those of CERES Terra EBAF Edition 2.6r OLR and OLR_{CLR}, henceforth
253 referred to as CERES OLR and OLR_{CLR}, for the overlap period starting September 2002 and
254 extending until June 2011. AIRS OLR and OLR_{CLR} products for parts of November 2003 and
255 January 2010 were missing from the daily AIRS data record because the AIRS instrument was
256 turned off on those days, and therefore observations for those days were not included in the
257 generation at the DISC of the monthly mean OLR and OLR_{CLR} values for these two months. We
258 used a procedure to generate approximate values of what AIRS monthly mean OLR products for
259 the months November 2003 and January 2010 would have been if the whole month had been
260 observed, and used these approximate values as if they were the observed values in subsequent
261 calculations. These approximated AIRS monthly mean data values were generated on a grid box
262 basis, by setting grid point differences between AIRS and CERES OLR for each of these
263 incomplete months equal to the average value of the corresponding AIRS/CERES differences for
264 the previous month and subsequent month, and adding these differences to the observed CERES
265 monthly mean products for each of the months in question. We used an analogous procedure to
266 synthesize the AIRS OLR_{CLR} data records for those two months.

267 We also synthesized some reported monthly mean CERES OLR_{CLR} data points for
268 individual ĺ x 1˚ grid boxes because these CERES OLR_{CLR} data values appeared to be
269 significant outliers when compared to nearby CERES OLR_{CLR} values, as well as with collocated
270 AIRS OLR_{CLR} values. For each grid box for each month, we eliminated any reported CERES

271 OLR_{CLR} value that differed by more than 20 W/m^2 from the corresponding AIRS OLR_{CLR} value.
272 We then spatially interpolated the remaining nearest values of the difference, CERES OLR_{CLR}
273 minus AIRS OLR_{CLR}, to synthesize approximate values of this difference for the grid boxes that
274 were found to be of questionable accuracy as described above, and then added the appropriate
275 differences to AIRS OLR_{CLR} for those grid boxes. Note that only 2.6% of the CERES OLR_{CLR}
276 monthly mean gridded values, which occurred primarily in the vicinity of Antarctica, were
277 synthesized in this manner and used in all subsequent calculations.

278 We observe a number of features in Figure 1a. The most prominent result is that to first
279 order, the AIRS and CERES OLR and OLR_{CLR} data sets appear biased compared to each other.
280 Figure 1b presents the differences between the AIRS and CERES monthly mean global mean
281 values of OLR and OLR_{CLR} shown in Figure 1a. The difference between AIRS Version-5 OLR
282 and CERES OLR shows a small annual cycle superimposed on a nearly constant bias. Part of
283 this annual cycle, with a maximum in June and a minimum in December, may be the result of the
284 large diurnal cycle of OLR over land. The CERES Science Team adjusts for the effects of the
285 diurnal cycle on CERES Terra observations as described in *Loeb et al*. [2012b, supplementary
286 information]. The AIRS monthly mean OLR product averages daytime and nighttime OLR
287 observations together but does not make any other correction for diurnal cycle. Figure 1b also
288 contains horizontal lines showing the average value of each difference. We show the average
289 value of the difference between AIRS and CERES OLR, computed over the eight year time
290 period September 2002 through August 2010, as a horizontal solid green line, with a value of
291 8.59 W/m^2. We computed this average difference over a full eight year period so as to minimize
292 the effect of the annual cycle on its value.

293 The differences between AIRS and CERES OLR_{CLR} are similar to, but smaller than,
294 those of OLR, with regard to both their mean value and their seasonal cycle. The mean value of
295 AIRS minus CERES Terra $OLR_{CLR,}$ shown as a horizontal solid red line, is 7.96 W/m^2. The
296 mean difference between AIRS and CERES OLR_{CLR} values is roughly 0.6 W/m^2 less than that of
297 AIRS and CERES OLR. The seasonal cycles of the differences between AIRS and CERES OLR
298 on the one hand, and AIRS and CERES OLR_{CLR} on the other, are displaced in time relative to
299 each other. This displacement might be a result of the significant sampling differences in the
300 cases included in the AIRS and CERES OLR_{CLR} data sets, respectively.

301 The large biases between the AIRS Version-5 OLR and OLR_{CLR} data records and those
302 of CERES are at first disconcerting but are readily understood. The AIRS OLR product derived
303 using the AIRS Science Team Version-6 retrieval algorithm is expected to have a much smaller
304 bias compared to CERES Terra OLR than does AIRS Version-5 OLR. The substantial, though
305 nearly constant, bias between OLR as computed from AIRS products and observed by CERES is
306 primarily a result of the use of the older set of line by line absorption coefficients in the
307 parameterization of the Version-5 OLR RTA [*Mehta and Susskind*, 1999a, 1999b], compared to
308 that used in the improved Version-6 OLR RTA [*Iacono et al*., 2008]. The main difference
309 between the two OLR parameterizations is that the *Iacono et al*. [2008] OLR RTA has more
310 absorption in the water vapor rotational band near 300 cm^{-1} than does that of *Mehta and Susskind*
311 [1999a]. As a result of this, a lower value of OLR will be computed for a given state in Version-
312 6, compared to that computed in Version-5, especially under very moist conditions. Global mean
313 total precipitable water vapor has an annual cycle, with more water vapor in the atmosphere in
314 the northern hemisphere summer, and less in the northern hemisphere winter, as compared to the
315 annual mean [*Vonder Haar et al., 2012*]. This phenomenon would contribute to the larger (more

316 positive) differences in the Version-5 OLR monthly mean products from the CERES OLR
317 monthly mean products in the northern hemisphere summer, and smaller (less positive) OLR
318 differences in the northern hemisphere winter, which is consistent with what is shown in Figure
319 1b.

320 We indicate monthly mean values of AIRS Version-6 OLR and OLR_{CLR} for the months
321 in which Version-6 was tested at JPL, excluding July 2011 and October 2011, in Figure 1a by
322 blue triangles and blue squares respectively. Figure 1b includes the monthly mean differences
323 between AIRS Version-6 OLR and CERES OLR for these months, shown in green triangles, and
324 the differences between AIRS Version-6 OLR_{CLR} and CERES OLR_{CLR}, shown in red squares.
325 The horizontal dashed green and red lines show the average values of the differences between
326 Version-6 OLR and CERES OLR, and Version-6 OLR_{CLR} and CERES OLR_{CLR}, with mean
327 differences of 3.50 W/m^2 and 1.02 W/m^2 respectively. We therefore expect from the results
328 shown in Figure 1b that AIRS Version-6 OLR and OLR_{CLR} time series will be significantly
329 closer to those of CERES Edition 2.6 than the corresponding time series of AIRS Version-5, at
330 least in the mean sense. Most of the remainder of this paper will discuss AIRS Version-5
331 products, including a comparison of monthly mean anomaly time series of AIRS Version-5 OLR
332 and OLR_{CLR} with those obtained from CERES. Anomaly time-series obtained from two different
333 sets of instruments can agree very well with each other even if the individual data sets are biased
334 against each other, provided the bias for a given month of the year is essentially constant in time.

335 5. Comparison of AIRS and CERES Global Mean and Tropical Mean Anomaly Time Series

336 We generated AIRS and CERES monthly mean OLR and OLR_{CLR} climatologies on a
337 1˚ x 1˚ spatial resolution for each month of the year by taking the average of the grid box value
338 for that month over an eight-year time period, i.e., the first eight consecutive Januaries, the first

339 eight consecutive Februaries, etc. The same ensembles of eight Januaries, Februaries, etc., are
340 used in the generation of climatologies for all products shown in this paper. OLR and OLR_{CLR}
341 anomalies for a given month in a given year, ǒn a 1 x 1˚ spatial grid, are defined as the
342 differences between their monthly mean values in that year and their monthly climatologies for
343 that grid box. The area mean anomaly for a given month is defined as the cosine latitude
344 weighted average of the grid box anomalies contained in the area under consideration.
345 Figure 2a shows the global mean anomaly time series of AIRS Version-5 OLR and
346 CERES OLR for the period September 2002 through June 2011, as well as the difference
347 between the two sets of monthly mean anomalies. Figure 2b shows analogous results for tropical
348 mean OLR anomalies, and Figures 2c and 2d show analogous global mean and tropical mean
349 anomaly time series for the AIRS and CERES OLR_{CLR} products. We define the term El Niño
350 Index as the difference of the NOAA monthly mean oceanic Sea Surface Temperature (SST),
351 averaged over the NOAA Niño-4 spatial area 5˚N to 5˚S latitude and 150˚W westward to 160˚E
352 longitude, from an eight year NOAA Niño-4 SST monthly mean climatology which we
353 generated based on use of the same eight years that we used in the generation of the OLR
354 climatologies. Figures 2b and 2d include the values of the El Niño Index multiplied by 1.5. All
355 anomaly time-series shown in Figures 2a-2d, as well as anomaly time series shown in subsequent
356 figures, have a linear three point smoother applied to them, in which the "smoothed" value of a
357 data point for a given month is represented as a weighted average of its value and those of the
358 neighboring months using a weight of 0.5 for the actual month and 0.25 for each of the
359 neighboring months.
360 Tropical mean OLR and OLR_{CLR} anomalies both tend to track those of the El Niño Index
361 in phase fairly closely, but the greatest tropical mean OLR anomalies are almost twice as large as

362 the greatest tropical mean OLR_{CLR} anomalies. Positive values of the El Niño Index (2003, 2005,
363 2007, early 2010) correspond to El Niño conditions, in which there are positive SST anomalies
364 in the Niño-4 area, and negative values (2008, mid-2010 to June 2011) correspond to La Niña
365 conditions, in which there are negative SST anomalies in the Niño-4 region. Figures 2a and 2c
366 show that an onset of negative global mean anomalies for both OLR and OLR_{CLR} began in late
367 2007. The negative tropical mean anomalies of both OLR and OLR_{CLR} shown in Figures 2b and
368 2d are generally considerably larger than the corresponding global mean anomalies, especially
369 after mid-2007. The decreases in global mean OLR and OLR_{CLR} in late 2007 are strongly
370 influenced by the significant reduction in tropical mean OLR and OLR_{CLR} which started a few
371 months earlier. Tropical mean OLR and OLR_{CLR} anomalies became positive starting in late
372 2009, roughly coincident with the onset of another El Niño event. Very substantial negative
373 global and especially tropical mean OLR anomalies occurred in the period starting mid-2010,
374 when the latest La Niña event began. This relationship between CERES OLR anomalies and El
375 Niño/La Niña activity has been documented in *Loeb et al.* [2012a, 2012b].

376 The difference between AIRS and CERES tropical mean OLR anomaly time series,
377 shown in green in Figure 2b, is generally in phase with the El Niño Index, with a temporal
378 correlation of 0.52. This is a result of fact that both positive and negative tropical mean AIRS
379 OLR anomalies are slightly larger in magnitude than those of CERES. An analogous result is
380 found with regard to the difference between AIRS and CERES global mean OLR, which has a
381 temporal correlation of 0.51 with the El Niño Index.

382 5.1 Average Rates of Change and El Niño Correlations of Anomaly Time Series

383 We define the Average Rate of Change (ARC) of an anomaly time series as the slope of
384 the linear least squares fit of the anomaly time series. We use the term Average Rate of Change

385 to describe the slope of an anomaly time series rather than the term trend, which is generally
386 used to characterize long-term multi-decadal data sets rather than the eight year 10 month period
387 studied in this paper. Figure 2b shows that the El Niño Index is highly non-linear over this time
388 period, with fluctuating values that are primarily positive at the start of the time period and
389 substantially negative at the end of the time period. The ARC of the El Niño Index, computed
390 over the time period September 2002 through June 2011, is -0.123 ± 0.046 K/yr. The
391 uncertainties shown here and subsequently represent twice the standard error, σ, of the regression
392 slope of the linear least squares fit [*Draper and Smith*, 1981]. The precise value of the ARC of
393 the El Niño Index, which depends on the beginning and end of the time period used in the
394 calculation, is less important than its sign, which shows that the Niño-4 region has cooled on the
395 average over the time period under study.

396 Spatial distributions of ARCs of OLR and other geophysical parameters, shown later in
397 the paper, are very coherent and are particularly informative with regard to the understanding of
398 why global mean and tropical mean OLR decreased over the period September 2002 through
399 June 2011. In this context, it is also very informative to examine the spatial distribution of
400 temporal correlations of 1˚ x 1˚ grid point anomaly time series with that of the El Niño Index.
401 We define these temporal correlations of anomaly time series around the earth with the single
402 anomaly time series of T_s averaged over the NOAA Niño-4 region as El Niño Correlations
403 (ENCs). ENCs are indicative of the agreement in both the phase and magnitude between the time
404 series of grid point anomalies and the El Niño Index. Unlike ARCs, ENCs should not depend
405 significantly on the precise beginning and end of the time series used to compute them if these
406 correlations hold up over long time periods. In those spatial areas in which the ARCs of OLR are
407 strongly influenced by El Niño/La Niña activity, there should be a very close agreement between

408 the spatial patterns of ARCs of OLR with those of the ENCs of OLR, and these patterns will be
409 of opposite sign as a result of the negative ARC of the El Niño Index.

410 Table 1a shows global mean and tropical mean values of the ARCs of AIRS OLR and
411 CERES Terra OLR anomalies over the time period September 2002 through June 2011, the
412 standard deviations between the two sets of global mean and tropical mean anomaly time series,
413 and the temporal correlations between each global mean and each tropical mean anomaly time
414 series. All statistics use values of the three point smoothed anomaly time series shown in Figure
415 2. The agreement of the ARCs of both global mean and tropical mean anomaly time series found
416 in the AIRS and CERES OLR records is on the order of ±0.03 $W/m^2/yr$, which is within the
417 uncertainty of the respective sets of ARCs. The temporal correlations of the AIRS and CERES
418 OLR anomaly time series with each other are 0.955 and 0.991 for global mean OLR and tropical
419 mean OLR respectively. Both AIRS and CERES OLR anomaly time series show that global
420 mean OLR has decreased on the average on the order of 0.075 $W/m^2/yr$ over the time period
421 September 2002 through June 2011, and that tropical mean OLR has decreased at a rate of
422 roughly -0.168 $W/m^2/yr$ from the beginning of the time period to the end. Demonstration of the
423 ability to obtain close agreement between global and tropical mean ARCs of AIRS and CERES
424 OLR anomaly time series, obtained in very different manners, is more significant than the values
425 of the ARCs themselves, which are influenced by the actual time period used in the
426 AIRS/CERES OLR data record comparison.

427 Table 1b shows analogous statistics comparing AIRS and CERES OLR_{CLR} anomaly time
428 series. The correlations between the AIRS and CERES OLR_{CLR} anomaly time series are still
429 high, but somewhat reduced from those of the OLR anomaly time series. In addition, the
430 standard deviations of the OLR_{CLR} anomaly differences are also somewhat larger than those of

OLR, and the global and tropical mean ARCs of OLR_{CLR} found in both data sets, while still negative, do not agree as closely as those of OLR. Nevertheless, the agreement obtained between anomaly time series of AIRS and CERES OLR_{CLR} is better than might be expected given the significant sampling differences between the cases included in each monthly mean OLR_{CLR} data set.

Table 1c shows temporal correlations between global mean and tropical mean anomaly time series of OLR and OLR_{CLR} as well as the correlations of the anomaly time series with the El Niño Index (ENCs). We show correlations using AIRS time series above the diagonal in bold and those using CERES time series beneath the diagonal. As shown in Table 1c, the temporal correlation between the CERES global and tropical mean OLR anomaly time series is 0.646, and the corresponding correlation for the AIRS anomaly time series is 0.705. This confirms that tropical anomalies provide a significant contribution to the global OLR anomaly time series found in both data sets. The CERES and AIRS tropical mean OLR anomaly time series also correlate very highly with the El Niño Index, with correlations greater than 0.8. CERES and AIRS tropical mean OLR_{CLR} anomaly time series also have high correlations with the El Niño Index, though somewhat smaller than those of the corresponding OLR data sets. Both sets of global OLR and OLR_{CLR} anomaly time series also show moderate correlations, on the order of 0.55, with the El Niño Index. These correlations of global and tropical anomaly time series with the El Niño Index further imply that the recent short term decreases in global and tropical OLR over the time period September 2002 through June 2011, as observed by both AIRS and CERES, are strongly influenced by changes from El Niño conditions at the beginning of the time series to La Niña conditions at the end. The comparisons shown in the remainder of this paper deal only with AIRS and CERES OLR anomaly time series.

454 5.2 The Spatial Distribution of ARCs and ENCs of OLR

455 This section compares the spatial distribution of ARCs of AIRS and CERES OLR with
456 each other on a 1˚ latitude by 1˚ longitude basis, as well as the spatial distribution of the
457 correlations of each anomaly time series with the El Niño Index (ENCs). These comparisons not
458 only show excellent agreement of ARCs and ENCs of AIRS OLR products with those of CERES
459 on a small spatial scale, but also depict the spatial regions that have been contributing
460 significantly to the short term decreases in global mean and tropical mean values of OLR over
461 the period under study.

462 All values for a given grid point shown in subsequent spatial plots such as Figures 3a-3d,
463 have a three point smoother applied to them in the latitude domain, as well as in the longitude
464 domain. These figures all contain boxes surrounding three areas. A box, shown in gray,
465 surrounds the NOAA Niño-4 region, 5˚N to 5˚S and 150˚W westward to 160˚E. A second box,
466 shown in black, lies to the west of the Niño-4 region and encompasses the area between 20˚N
467 and 20˚S from 90˚E eastward to 135˚E. Much has been written about the meteorology of this
468 region, which includes the Maritime Continent and the Western Pacific Warm Pool, as well as
469 Darwin Australia, particularly with regard to its response to El Niño/La Niña activity. In
470 particular, the Southern Oscillation Index (SOI), which represents the monthly mean value of
471 Tahiti sea level pressure minus that of Darwin, is well known to be strongly anti-correlated with
472 SST anomalies in the region of El Niño activity, and the two phenomena are often linked
473 together with the single acronym El Niño/Southern Oscillation (ENSO). We will refer to the area
474 encompassed by this box as the Warm Pool Maritime Continent (WPMC region). A third box,
475 also shown in black, covers portions of the eastern tropical Pacific Ocean, northern South
476 America, and the equatorial Atlantic Ocean and is the composite of three adjacent rectangles:

5˚N to 20˚S, 140˚W to 95˚W; 8˚N to 20˚S, 95˚W to 70˚W; and 8˚N to 8˚S, 70˚W to 10˚E. We will refer to the area encompassed by these three contiguous rectangles as the Equatorial Eastern Pacific and Atlantic (EEPA) region. Less attention has been paid to the meteorology of this region and its response to El Niño, especially the Atlantic Ocean portion of the EEPA region.

The global spatial distributions of OLR ARCs over the time period September 2002 through June 2011 are shown in Figures 3a and 3b for AIRS and CERES, respectively. As discussed previously, more significant than the precise values of the ARCs shown in Figure 3 is the very coherent spatial structure of the ARCs of OLR. Figures 3a and 3b demonstrate two very important points. The first is the virtually indistinguishable spatial distributions of the ARCs of AIRS OLR and of CERES OLR. Figure 3c shows their difference, with a spatial correlation of 0.99 between the ARCs of the two OLR data sets, and a standard deviation of 0.11 $W/m^2/yr$. The global mean AIRS OLR ARC for this period is 0.035 $W/m^2/yr$ lower (more negative) than that of CERES. This small difference in OLR ARCs is not uniform, but occurs primarily near 30˚S latitude, especially over Eastern Australia in which the large negative ARCs of OLR are greater in AIRS than in CERES. The same negative difference in OLR ARCs is also observed in another region near 30S, extending from 120˚W eastward to about 50˚W, in which both AIRS and CERES OLR ARCs are positive.

The most important scientific point of Figures 3a and 3b is that while the global mean and tropical mean ARCs of OLR are negative, there is considerable spatially coherent longitudinal structure of the ARCs of OLR at a given latitude, with differing signs and amplitudes. This structure is largest in the tropics, but is found at other latitudes as well. Figure 3 shows that positive OLR ARCs as large as 4.2 $W/m^2/yr$ exist in the vicinity of the equatorial dateline, including and surrounding the Niño-4 region. These are more than compensated for, in

500 the tropical mean sense, by negative OLR ARCs at other longitudes, as large as – 3.2 W/m^2/yr
501 near the equator over Indonesia, in the vicinity of 120˚E longitude, which lies within the WPMC
502 region. Indeed, ARCs of OLR within the entire WPMC region are very negative over the period
503 September 2002 through June 2011. ARC's of OLR within the spatially larger EEPA region are
504 also negative over this time period though less so than over the WPMC region. As demonstrated
505 in Figure 3, the ARC of OLR over Darwin, contained within the WPMC region, is opposite in
506 sign to that of Tahiti, near 18˚S and 150˚W. As stated previously, tropical OLR in a given region
507 will decrease with increasing convective activity, which leads to both increases in mid-
508 tropospheric water vapor as well as more high clouds. Increasing convective activity in a given
509 region is also associated with decreases in sea level pressure in that region. The reverse
510 phenomena will occur in the case of increasing subsidence in a given region.
511 There are many possible factors contributing to the patterns of spatial distribution of the
512 relatively small differences of AIRS OLR ARCs and CERES OLR ARCs shown in Figure 3c.
513 Our analysis of the twelve months in which Version-6 OLR products were generated indicates
514 that the agreement of spatial patterns of AIRS Version-6 OLR ARCs with those of CERES will
515 be even better than what was obtained using Version-5. We approximated what the difference
516 would be of Version-5 OLR ARCs from those obtained using Version-6, on a grid point basis, by
517 taking the slope of the linear least squares fit of Version-5 OLR minus Version-6 OLR, as a
518 function of time, for each of the 12 months in which Version-6 products were generated. Spatial
519 patterns of these approximated differences in OLR ARCs are shown in Figure 3d. There is a
520 remarkable similarity in the spatial patterns of OLR ARC differences shown in Figures 3c and
521 3d. This indicates that the differences between Version-6 OLR ARCs and those of CERES will
522 be even smaller than those found with regard to Version-5 OLR, because a large part of the grid

523 point differences between AIRS and CERES OLR ARCs will be accounted for using ARCs of
524 AIRS Version-6 OLR.

525 Figures 4a-4c are analogous to Figures 3a-3c but show patterns of ENCs of AIRS and
526 CERES OLR and their difference. ENCs represent correlations and are therefore unitless, with
527 values ranging from -1.0 to 1.0. The color scales of Figures 4a, 4b, and 4c are reversed from
528 those of Figures 3a, 3b, and 3c because regions of positive (negative) ARCs generally
529 correspond to regions of negative (positive) ENCs. As found with regard to ARCs of OLR, there
530 is again considerable spatial structure, and excellent agreement, in the ENCs of AIRS and
531 CERES OLR, with a global spatial correlation of 0.97. This agreement shows that not only are
532 the slopes of high spatial resolution anomaly time series of AIRS and CERES OLR in close
533 agreement with each other, but implies that the anomaly time series themselves are also in close
534 agreement.

535 The spatial structure of ENCs of OLR closely follows that of the OLR ARCs but with
536 opposite sign (that is, contains similar colors), especially in the tropics. For example, the area of
537 large positive ARCs of OLR including and surrounding the NOAA Niño-4 region, shown in
538 green and red in Figures 3a and 3b, has OLR anomalies which are strongly anti-correlated with
539 the El Niño Index, and are also shown in green and red in Figures 4a and 4b. This demonstrates
540 that periods of positive SST anomalies in the Niño-4 region correspond to negative OLR
541 anomalies in the Niño-4 region and surrounding areas. The reverse situation is found within the
542 WPMC and EEPA regions, which contain blue and yellow colors in both Figures 3a and 3b as
543 well as in 4a and 4b, indicative of substantial negative OLR ARCs and substantial positive OLR
544 ENCs in these regions. This anti-correlation of the spatial distributions of ARCs and ENCs of
545 tropical OLR between September 2002 and June 2011 indicates that the tropical ARCs of OLR

546 shown in Figure 3 are very strongly influenced by time periods containing significant El Niño/La
547 Niña activity.

548 The inverse relationship between spatial patterns of ARCs and ENCs holds in some
549 extra-tropical areas as well. Globally, the spatial distribution of ARCs and ENCs of OLR have
550 correlations with each other of -0.78 and -0.79 for AIRS and CERES, respectively. It is
551 interesting to note that differences between ARCs of AIRS and CERES OLR (Fig. 3c) are also
552 anti-correlated with (that is, have similar colors to) the differences in their ENCs (Fig. 4c), which
553 shows that AIRS tropical OLR anomaly correlations with El Niño activity are slightly higher
554 than CERES OLR anomaly correlations, thus resulting in slightly more negative tropical mean
555 ARCs of AIRS OLR compared to CERES, as shown in Table 1a.

556 Figures 4a and 4b are very similar in appearance to Figure 3 of *Davies and Molloy*
557 [2012], which shows the spatial distribution of the temporal correlation of cloud top height
558 anomalies H′ derived from Multiangle Imaging Spectro-Radiometer (MISR) with the SOI over
559 the period 2000 through 2010. *Davies and Molloy* have red colors showing negative correlations
560 of cloud height anomalies H′ with the SOI. The agreement of colors in Figures 4a with those of
561 *Davies and Molloy* [2012] is expected because OLR decreases with increasing H′ on the one
562 hand, and the SOI is out of phase with the El Niño Index on the other.

563 The spatial correlations of the anomaly time series of AIRS OLR with those of CERES
564 OLR for each 1˚ by 1˚ grid point are shown in Figure 4d. The global mean AIRS/CERES OLR
565 anomaly time series correlation, on a 1˚ x 1˚ spatial scale, is 0.93, with the largest differences
566 occurring in the mid-latitudes and over convective areas in South America and Africa. This
567 shows that as with their ARCs and ENCs, AIRS and CERES OLR anomaly time series on a 1˚
568 x 1˚ spatial scale also agree closely with each other.

569 Table 1a shows that both AIRS and CERES OLR anomaly time series confirm that global
570 mean and especially tropical mean OLR decreased over the time period under study. As depicted
571 in Figure 3, the largest OLR ARCs occur in the tropics within the WPMC region and near the
572 dateline surrounding the Niño-4 region. OLR ARCs in these areas are roughly equal to each
573 other and of opposite sign. The effects of the large positive and negative tropical OLR ARCs
574 near the dateline and over the WPMC region tend to cancel in the zonal mean sense. The first 3
575 lines of Table 2 show values of ARCs and ENCs of OLR averaged over different spatial regions
576 related to the WPMC region, as determined using each of the AIRS and CERES OLR data sets.
577 The first line of Table 2 shows statistics related to ARCs and ENCs of OLR computed only
578 within the WPMC region. AIRS and CERES both show very large negative ARCs and very high
579 positive ENCs of OLR within this region. The second and third lines of Table 2 show values of
580 global and tropical mean ARCs and ENCs of OLR computed only over areas outside of the
581 WPMC regions. The tropical mean OLR ARC over the period September 2002 through June
582 2011, computed as previously, but after replacing OLR ARCs in the WPMC region by zeroes, is
583 0.004 ± 0.054 W/m^2/yr for AIRS and 0.034 ± 0.053 W/m^2/yr for CERES. Both of these values
584 are essentially zero, given their uncertainties. In addition, ENC's of tropical mean OLR outside
585 of the WPMC region are both very low. Likewise, the global mean AIRS OLR ARC, computed
586 after excluding ARCs within the WPMC region, is -0.030 ± 0.028 W/m^2/yr, and is 0.005 ± 0.027
587 W/m^2/yr for CERES, again both essentially zero. This indicates that both OLR data sets show
588 that a substantial part of the recent negative global mean and tropical mean OLR ARCs results
589 from the contribution of OLR anomalies contained within the WPMC region to the overall
590 statistics. These statistics can give rise to the misleading conclusion that the response of OLR

591 within the WPMC region to El Niño activity is the sole cause of the fact that tropical and global
592 mean OLR anomalies are strongly correlated with El Niño/La Niña. This is not the case.

593 Figure 3 shows that OLR ARCs are negative over the EEPA region as well. While ARCs
594 of OLR over the EEPA region are not as negative as those over the WPMC region, the spatial
595 extent of the EEPA region is considerably larger than that of the WPMC region. The last three
596 lines of Table 2 show statistics for OLR anomalies computed both within and outside of the
597 EEPA region analogous to those shown for the WPMC region. Exclusion of OLR within the
598 EEPA region from the calculations of otherwise global and tropical mean ARCs likewise
599 accounts for most of the negative ARCs of global and tropical mean OLR found during the
600 period under study. The fact that OLR has been decreasing over the study period, and that OLR
601 anomalies are strongly correlated with the El Niño Index over this period, is not the result of
602 OLR changes within either the WPMC region or the EEPA region. Rather, it is the result of the
603 fact that there are two such regions in the tropics, one to the east and one to the west of the
604 Niño-4 region, in which OLR anomalies are each out of phase with, and individually compensate
605 for, those in the Niño-4 region.

606 5.3. Longitudinal Distribution of Equatorial Anomaly Time Series: Hovmöller Diagrams

607 Figures 3 and 4 show that the tropics contain large spatially coherent areas with
608 alternating values of positive and negative ARCs and ENCs of OLR over the time period under
609 study. Figures 5a and 5b present Hovmöller diagrams showing time series of monthly mean
610 AIRS and CERES OLR anomalies (vertical scale), integrated over the latitude range 5˚N through
611 5˚S, in each 1˚ longitude bin (horizontal scale) for the time period September 2002 through June
612 2011. These Hovmöller diagrams demonstrate the origin of the ARCs and ENCs of near
613 equatorial OLR shown in Figures 3 and 4. The difference between the AIRS OLR Hovmöller

614 diagram and the CERES OLR Hovmöller diagram is shown in Figure 5c. Figures 5a and 5b, and
615 all subsequent Hovmöller diagrams, have a small amount of smoothing applied to them. A five
616 point (five month) linear smoothing was applied in the vertical and a 15 point (15 degree) linear
617 smoothing was applied in the horizontal to minimize the effects of small discontinuities between
618 adjacent rectangular grid points on the figures. Most of the Hovmöller domain 5˚N to 5˚S is
619 ocean. There are three relatively small land areas near the equator: South America, Africa, and
620 Indonesia. These land areas each lie between the three sets of thin black vertical lines shown in
621 Figure 5. The longitudinal extent of the Niño-4 region is also indicated in Figure 5 by two
622 vertical gray lines.

623 AIRS and CERES Hovmöller diagrams of tropical OLR anomalies are essentially
624 identical, with a correlation coefficient of 0.995 between them. Some of the largest differences
625 between the AIRS and CERES tropical anomaly time series occur in November 2003 and
626 January 2010, the two months for which AIRS data was synthesized. The differences between
627 AIRS and CERES in these two months would have been much larger if the AIRS "monthly
628 mean" OLR products stored at the GES DISC were used in the calculations, as was done
629 originally. In both cases, the AIRS "monthly mean" products of the DISC represented averages
630 over less than a month time period, while the CERES data represented observations taken over
631 the entire month. The fact that the remainder of the OLR anomaly differences shown in Figure
632 5c were so small alerted us to check, and correct for, the cause of the problem found in the data
633 obtained from the GES DISC for these two months.

634 The anomaly time series shown in Figure 5 depict the phase relationship of OLR
635 anomalies at different longitudes in the vicinity of the equator as a function of time. Such figures
636 provide insight into the spatial distribution of tropical ARCs and ENCs of OLR in the vicinity of

637 the equator shown in Figures 3 and 4. In the Niño-4 region, equatorial OLR anomalies were very
638 negative in late 2002/early 2003, which corresponds to an El Niño period. Very positive OLR
639 anomalies in the Niño-4 region occur from mid-2007 through early 2009 and mid-2010 through
640 June 2011, both during La Niña periods. These features give rise to the substantial positive OLR
641 ARC shown in Figures 3a and 3b over the Niño-4 region. Figure 3 shows very negative values of
642 OLR ARCs near the equator between 90˚E and 135˚E longitudes, within the WPMC region.
643 Figure 5 shows that equatorial OLR anomalies between 90˚E and 135˚E are out of phase with
644 those in the Niño-4 region and are of comparable magnitude. Figure 5 also shows that equatorial
645 OLR anomalies from 140˚W eastward to 10˚E, within the longitudinal domain of the EEPA
646 region, tend to be smaller than, and out of phase with, those in the Niño-4 region, especially
647 during La Niña periods. This phenomenon gives rise to the negative equatorial OLR ARCs
648 shown in Figure 3 contained within the EEPA region. The phase relationships discussed above
649 are also reflected in the ENCs of equatorial OLR shown in Figure 4.

650 Figures 3 to 5 show that the spatial patterns of both the Average Rates of Change and El
651 Niño Correlations of OLR over the time period September 2002 through June 2011, as observed
652 by AIRS and CERES, are in excellent agreement with each other, as are their equatorial anomaly
653 time series in the vicinity of the equator. Both CERES and AIRS OLR products show that the
654 period September 2002 through June 2011 is marked by a substantial decrease in global mean
655 OLR, on the order of−0.075 $W/m^2/yr$, and a larger decrease in tropical mean OLR on the order
656 of −0.165 $W/m^2/yr$. This agreement of Average Rates of Change of OLR anomaly time series,
657 derived from observations by two different instruments, in totally independent and different
658 manners, implies that both sets of OLR products must be stable over the eight year 10 month
659 period in which they were compared. There should be little question that there actually was a

significant decrease of global mean OLR over the time period September 2002 through June 2011, and that the majority of the decrease occurred in the tropics.

These results, found by both CERES and AIRS, should not be taken as indicative of what will happen in the future. It mainly shows that OLR anomalies and their Average Rates of Change can be determined very accurately by two totally independent instrumental and theoretical approaches. The agreement of anomaly time series of OLR as determined using CERES and AIRS observations also indirectly validates the anomaly time series of the AIRS derived products used in the computation of AIRS OLR, at least for the time period September 2002 through June 2011. The next section uses anomaly time series of AIRS derived products to explain the factors contributing to the anomaly time series of OLR over the period under study and why OLR anomalies are strongly correlated with the El Niño Index.

6. The Effect of Phases of El Niño/La Niña on Tropical Water Vapor, Cloud Cover, and OLR Anomaly Time Series

As discussed previously, OLR increases with both increasing skin temperatures T_s as well as with increasing temperature profile $T(p)$, and in general, everything else being equal, decreases with increasing radiatively effective cloud fraction $\alpha\varepsilon$ and with increasing water vapor $q(p)$. It is impractical to show results relating to anomaly time series of all the important geophysical parameters affecting those of OLR. In this paper, for demonstrative purposes, we concentrate on T_s, 500 mb specific humidity which we refer to as q_{500}, and $\alpha\varepsilon$. The OLR calculations of course take into account the detailed changes in the entire water vapor profile and the heights and amounts of clouds, as well as those of the temperature and ozone profiles on which OLR also depends. To first order, OLR responds linearly to changes in T (ΔT) and $\alpha\varepsilon$

682 *(Δαε)*, and in the case of water vapor q, OLR responds linearly to changes in $\ell n(q)$ $(\Delta \ell n(q))$,
683 which corresponds to percent change in q $(\Delta q/q)$.

684 Figures 6a and 6b show the spatial distribution of the ARCs and ENCs of AIRS
685 Version-5 T_s over the period September 2002 through June 2011. As with OLR, the monthly
686 mean anomaly used in the computation of ARCs and ENCs of T_s is given by the difference of the
687 monthly mean value of T_s for a given year from its climatological value. The color code used in
688 Figure 6a, showing ARCs of T_s, is analogous to that used in Figure 3, showing ARCs of OLR,
689 with positive values depicted in reds and greens, and negative values depicted in blues and
690 yellows. In addition, as with Figures 4a and 4b, red and green colors in Figure 6b indicate
691 negative ENCs, and blue, yellow, and orange colors indicate positive ENCs.

692 A number of important features are found in Figure 6a. While the global mean ARC of T_s
693 is essentially zero over this time period, there are areas in which significant positive and negative
694 T_s ARCs exist. There has been considerable warming near the North Pole over this time period,
695 as well as considerable warming and cooling in different areas over Northern Hemisphere extra-
696 tropical land. In addition, there has been substantial cooling over much of Africa, especially
697 south of 15˚S, as well as over much of Australia. All of these areas in which extra-tropical land
698 has either warmed or cooled considerably over the time period under study are also characterized
699 by increases or decreases in OLR as shown in Figure 3. This is consistent with the fact that
700 everything else being equal, increases (decreases) in T_s result in increases (decreases) in OLR.

701 Another prominent feature shown in Figure 6a is that the tropics are marked by
702 substantial oceanic surface temperature cooling within and immediately surrounding the Niño-4
703 region encompassed by the gray rectangle. This area of oceanic cooling over the last nine years
704 is surrounded to the south, west, and north by areas in which oceanic warming has occurred

705 during this period, though to a lesser extent. Figure 3 shows that OLR changes in these oceanic
706 areas are considerable, and unlike over extra-tropical land, are of opposite sign to those of the
707 changes in T_s. This indicates that the changes in tropical oceanic OLR in these regions are driven
708 primarily by changes in water vapor profile and cloud cover rather than by changes in T_s.

709 Figure 6b shows that, as is the case with regard to OLR, ENCs of T_s are generally of
710 opposite sign (similar color) to their ARCs. The global mean spatial correlation of ARCs and
711 ENCs of T_s with each other is -0.56, which is still appreciable but smaller than that for OLR. It is
712 apparent from Figures 6a and 6b that the considerable cooling of T_s that took place over South
713 Africa and Australia is related to a strong in phase relationship of T_s with El Niño/La Niña
714 activity in these areas. On the other hand, the significant changes in T_s that occurred over
715 Northern Hemisphere extra-tropical land, such as the warming that occurred near the North Pole,
716 are not closely related to El Niño activity, at least in an unlagged sense, because ENCs of T_s in
717 these areas are not appreciable. It is also interesting to note that in some equatorial oceanic areas,
718 such as in the vicinities of 90˚W and 60˚E, T_s anomalies had moderate positive correlations with
719 the El Niño Index but T_s in those areas had very small Average Rates of Change. In addition,
720 while ARCs and ENCs of OLR within the WPMC region and the EEPA region were all large
721 and of the same sign, this is not the case with regard to T_s in these regions.

722 Figures 6c and 6d show ENCs of q_{500} and $\alpha\varepsilon$ respectively. With regard to q_{500}, the
723 monthly mean anomalies used in the generation of ARCs and ENCs are in units of % change and
724 are given by $[(q_{500} - q_{500}{}^{clim})/q_{500}{}^{clim}]$ where $q_{500}{}^{clim}$ is the monthly climatological value of q_{500} for
725 that grid box. This is the appropriate value to use because, as stated previously, changes in OLR
726 are linear to first order with changes in $\ell n(q)$. Anomalies of $\alpha\varepsilon$ are treated analogously to those

727 of OLR and T_s. In the tropics, ARCs of q_{500} and $\alpha\varepsilon$ (not shown) are out of phase with ENCs of
728 these parameters, as was the case with ARCs and ENCs of OLR. ENCs of q_{500} and $\alpha\varepsilon$ are each
729 very positive in the Niño-4 region, as are ENCs of T_s. These high positive correlations with the
730 El Niño Index indicate that a significant overall mid-tropospheric drying and a corresponding
731 overall decrease in cloud cover occurred in the Niño-4 region over the period under study. An
732 analogous situation occurred in the areas of warming surface skin temperature surrounding the
733 Niño-4 region, in which ENCs of q_{500} and $\alpha\varepsilon$ are very negative, indicative of considerable mid-
734 tropospheric moistening as well as increasing cloud cover in these surrounding regions during
735 the period under study. Unlike T_s, however, there are also large negative ENCs of q_{500} and $\alpha\varepsilon$
736 contained within most of the WPMC and the EEPA regions over this time period, indicative of
737 both considerable mid-tropospheric moistening and increasing cloud cover over these two
738 regions. Of particular significance are the large negative ENCs of cloud fraction, and even more
739 so, of 500 mb specific humidity, contained within the EEPA region off the West Coast of South
740 America, indicative of both moistening and increased cloudiness in this area over the time period
741 under study. This phenomenon is what gave rise to the large positive ENCs and large negative
742 ARCs of OLR off the west coast of South America, as shown in Figures 4 and 3 respectively.
743 Hovmöller diagrams provide a good depiction of the interrelationship of equatorial
744 anomalies of different geophysical parameters as a function of time and longitude, as discussed
745 above. The Hovmöller diagram of monthly mean AIRS T_s anomalies (K) for the period
746 September 2002 through June 2011 is shown in Figure 7a, and those of $q_{500}(\%)$ and $\alpha\varepsilon(\%)$ are
747 shown in Figures 7b and 7c. As in Figure 5, the vertical gray lines in Figure 7 delineate the
748 longitudinal band containing the Niño-4 region, 150˚W longitude westward to 160˚E. Figure 7a
749 clearly demonstrates that the large negative T_s ARC in the Niño-4 region, shown in Figure 6a, is

750 the result of the transition from an El Niño condition (locally positive T_s anomaly) at the end of
751 2002 to La Niña conditions (locally negative T_s anomalies) over the time periods late 2007
752 through 2008, and especially late 2010 through mid-2011. Equatorial T_s anomalies between
753 100˚E and 140˚E, within the WPMC region, tend to be smaller than, and of opposite sign to,
754 those in the vicinity of the dateline. This gives rise to the band of weaker positive T_s ARCs near
755 the equator from 100˚E to 140˚E shown in Figure 6a. T_s anomalies in the equatorial Atlantic
756 Ocean are also to some extent out of phase with those in the Niño-4 region, resulting in the small
757 positive ARCs, and moderately negative ENCs, of T_s in the equatorial Atlantic Ocean as shown
758 in Figures 6a and 6b.

759 Anomalies of q_{500} and $\alpha\varepsilon$ within the Niño-4 region generally follow those of T_s very
760 closely, both in magnitude and in phase. This indicates, not surprisingly, that positive SST
761 anomalies in the Niño-4 region correspond to periods of increased convection in that area,
762 leading to enhancement of moisture in the mid-troposphere as well as increases in cloud cover.
763 Conversely, negative SST anomalies in the Niño-4 area correspond to periods of decreased
764 convection (increased subsidence) leading to periods of a drier mid-troposphere and decreases in
765 cloud cover. Water vapor and cloud cover anomalies in the WPMC region, from roughly 90˚E to
766 135˚E, are out of phase with those near the dateline, as was found for T_s. Unlike T_s anomalies in
767 the WPMC region, which were smaller than those near the dateline, q_{500} and $\alpha\varepsilon$ anomalies in the
768 WPMC region are closer in magnitude to those near the dateline. This is the result of the
769 westward shift of the area of maximum convection during La Niña periods from the dateline to
770 the WPMC region. This out-of-phase relationship gives rise to the very substantial negative
771 ENCs of q_{500} and $\alpha\varepsilon$ over Indonesia during this time period, as depicted in Figures 6c and 6d.

772 Figures 6c and 6d contain substantial negative ENCs of q_{500} and $\alpha\varepsilon$ in some tropical
773 locations in which no significant changes in T_s exist. The most notable of these is off the west
774 coast of South America, in the vicinity of 5˚N to 20˚S from 120˚W eastward to 80˚W, which is a
775 part of the EEPA region. There is also another region of positive q_{500} ENCs near the equator
776 going across South America and extending eastward along the Atlantic Ocean to about 10˚E
777 longitude, which is also contained within the EEPA region. Figures 7b and 7c show that
778 equatorial water vapor and cloud cover anomalies off the west coast of South America are often
779 out of phase with those at the dateline, especially during the large La Niña events in 2007-2008
780 and 2010-2011. This demonstrates that La Niña periods of decreased convection near the
781 dateline also correspond to periods of increased convection eastward of 120˚E, as a result of the
782 eastward shift of the convective branch of the Walker circulation during La Niña periods [*Power*
783 *and Smith*, 2007; *Zhou et al*., 2011]. The same relationship is found to a lesser extent over the
784 Atlantic Ocean extending to 10˚E longitude at the eastern end of the EEPA region.
785 The Hovmöller diagrams of q_{500} and $\alpha\varepsilon$, shown in Figures 7b and 7c, are both strongly
786 anti-correlated with that of OLR, shown in Figure 5. The Hovmöller diagrams of q_{500} and $\alpha\varepsilon$
787 have correlations with those of AIRS OLR of -0.79 and -0.93 respectively, and have correlations
788 of -0.79 and -0.92 with those of CERES OLR. This further demonstrates that anomalies in
789 tropical mid-tropospheric water vapor, and especially in cloud cover, are the driving forces
790 behind changes in tropical OLR.
791 The previous discussion was related primarily to the tropics. Figures 6a and 6b also show
792 that spatial patterns of ENCs of q_{500} and $\alpha\varepsilon$ over the entire latitude range 60˚N to 60˚S are in
793 general similar to each other. Note, for example, that the large negative ENCs of q_{500} and $\alpha\varepsilon$
794 found over the WPMC region each extend southeastward toward and beyond the southern tip of

South America. In addition, the large positive ENCs of q_{500} and $\alpha\varepsilon$ found over the Niño-4 region continue toward and across southern South America in the area that lies immediately to the north of that described above. Similar features appear in the spatial distributions of the ARCs of q_{500} and $\alpha\varepsilon$, which are not shown in this paper. In addition, these same features are found, with reversed colors, in the ARCs of AIRS and CERES OLR shown in Figures 3a and 3b because increases in q_{500} and $\alpha\varepsilon$ tend to result in decreases in OLR.

An examination of the small differences between the ARCs of AIRS and CERES OLR shown in Figure 3c, which we will refer to as ΔOLR ARC, also shows similar patterns to those found in the ENCs (as well as in the ARCs) of $\alpha\varepsilon$. Figure 8 depicts the relationship between ΔOLR ARC and $\alpha\varepsilon$ ARC in terms of a scatter diagram relating values of these two quantities for all grid points 60˚N to 60˚S. It is apparent from Figure 8 that there is a tendency for grid points with positive ARCs of $\alpha\varepsilon$ to be more associated with those having negative values of ΔOLR ARC, with the reverse being true for grid points with negative ARCs of $\alpha\varepsilon$. The blue line shows the linear least squares fit through the points shown in the figure, which has a slope of -0.0743 ± 0.0028 $(W/m^2/yr)/(\%/yr)$.

At least part of this correlation between ARCs of cloud cover and the difference between ARCs of AIRS and ARCs of CERES OLR is a result of the fact that the Version-5 AIRS OLR RTA does not account for enough absorption in the water vapor rotational band. This is the main reason that computed AIRS Version-5 OLR values are biased high compared to CERES OLR. For a given scene, the error in the computation of AIRS Version-5 OLR will tend to decrease with increasing cloud cover, especially for high clouds, because clouds obscure a substantial portion of the water vapor in the scene. Consequently, for more cloudy cases, AIRS computed Version-5 OLR is closer to the value observed by CERES than for less cloudy cases. Increasing

818 cloud fraction over time for a given grid box therefore results in decreasing the (positive)
819 computed differences of AIRS OLR relative to the CERES OLR, while simultaneously
820 producing a negative contribution to AIRS OLR anomalies which are computed relative to the
821 more positive AIRS climatology. Our preliminary estimate of how Version-6 OLR ARCs will
822 differ from those of Version-5, shown in Figure 3d, indicates that spatial differences between the
823 ARCs of AIRS Version-6 OLR and those of CERES OLR should indeed be even smaller than
824 those between Version-5 OLR and CERES OLR.

825 7. Summary

826 The first part of this paper compared September 2002 through June 2011 anomaly time
827 series of OLR and OLR_{CLR} data records, determined from CERES observations as generated by
828 the CERES Science Team, and from AIRS observations as generated by the AIRS Science
829 Team. Excellent agreement was found between the CERES and AIRS OLR anomaly time series
830 down to the 1˚ latitude by 1˚ longitude spatial scale. CERES and AIRS data records both show
831 that global mean and tropical mean OLR have decreased over the time period under study, and
832 more significantly, that both global and tropical mean OLR anomaly time series are strongly
833 correlated with El Niño/La Niña variability as expressed by the El Niño Index as defined in this
834 paper. This high correlation, as well as the decrease in global and tropical mean OLR over the
835 time period under study, was shown to result primarily from changes in mid-tropospheric water
836 vapor and cloud cover in two equatorial regions, one to the east of, and one to the west of, the
837 Niño-4 region, both in response to El Niño/La Niño activity.

838 The AIRS results shown in this paper were based on products derived using the AIRS
839 Science Team Version-5 retrieval algorithm. The AIRS Version-6 retrieval algorithm is expected
840 to become operational in late 2012, and will be used to analyze all future AIRS observations as

well as to reanalyze all previous AIRS observations. AIRS Version-6 OLR and OLR_{CLR} data records should be much closer in the mean to those of CERES, and in addition, it is expected that AIRS Version-6 OLR ARCs will show even better agreement with CERES OLR ARCs than that found in AIRS Version-5. AIRS Version-6 data records will also include monthly mean values of the spectral components of OLR averaged over each of the 16 contiguous spectral bands used in the computation of OLR in Version-6. Anomaly time series of OLR computed only over each of these spectral intervals, and the spatial distribution of their Average Rates of Change and El Niño Correlations, will provide important additional information to help understand the effect of El Niño/La Niña oscillations on OLR. We plan to conduct further studies comparing AIRS Version-6 OLR with CERES OLR products as well as evaluating ARCs and ENCs of the spectral components of AIRS OLR.

The results shown in this paper should not be taken as to be indicative of how OLR will change in the future, especially with regard to possible increases or decreases in global mean OLR. The EOS satellites carrying AIRS and CERES are expected to last about 20 years. A 20 year time series of overlapping AIRS and CERES OLR data records would be a very useful first step towards monitoring and understanding long term variability and possibly drifts of OLR.

References:

Allan, R. P., and M. A. Ringer (2003), Inconsistencies between satellite estimates of longwave cloud forcing and dynamical fields from reanalyses, *Geophys. Res. Lett.*, *30***,** 4.

Barkstrom, B., E. Harrison, G. Smith, R. Green, J. Kibler, R. Cess, the ERBE Science Team (1989), Earth Radiation Budget (ERBE) archival and April 1985 results, *Bull. Am. Meteorol. Soc.*, *70*, 1254-1262.

867

868 Barlow, M., M. Wheeler, B. Lyon, and H. Cullen (2005), Modulation of daily precipitation over
869 Southwest Asia by the Madden-Julian Oscillation, *Mon. Weather Rev.*, *133*, 3579-3594.
870

871 Brown, J. R., S. B. Power, F. P. Delage, R. A. Colman, A. F. Moise, B. F. Murphy (2011),
872 Evaluation of the South Pacific Convergence Zone in IPCC AR4 Climate Model Simulations of the
873 Twentieth Century, *J. Clim.*, *24*, 1565-1582, doi:10.1175/2010JCLI3942.1.
874

875 Chiodi, A. M., and D. E. Harrison (2010), Characterizing warm-ENSO variability in the equatorial
876 Pacific: An OLR perspective, *J. Clim.*, *23*, 2428-2439.
877

878 Chu, P. S., and J. B. Wang (1997), Recent climate change in the Tropical Western Pacific and Indian
879 Ocean Regions as detected by Outgoing Longwave Radiation records, *J. Clim.*, *10*, 636-646.
880

881 Chung, E. S., D. Yeomans, and B. J. Soden (2010), An assessment of climate feedback processes
882 using satellite observations of clear-sky OLR, *Geophys. Res. Lett.*, *37*, 7.
883

884 Clement, A. C., B. Soden (2005), The sensitivity of the Tropical-Mean Radiation Budget, *J. Clim.*,
885 *18*, 3189-3203, doi: 10.1175/JCLI3456.1.
886

887 Davis, R. and M. Molloy (2012), Global cloud height fluctuations measured by MISR on Terra from
888 2000 to 2010, *Geophys. Res. Lett.*, *39*, L03701, doi:10.1029/2011GL050506.
889

890 Dessler, A. E., Z. Zhang, and P. Yang (2008), Water-vapor climate feedback inferred from climate
891 fluctuations, 2003-2008, *Geophys. Res. Lett*., *35*, L20704, doi: 10.1029/2008GL035333.

892

893 Dessler, A. E. (2010), A determination of the cloud feedback from climate variations over the past
894 decade, *Science*, *330*, 1523-1527, doi: *10.1126/science.1192546*
895
896 Doelling, D. R., N. G. Loeb, D. F. Keyes, M. K. Nordeen, D. Morstad, B. A. Wielicki, D. F. Young,
897 and M. Sun (2012), Geostationary enhanced temporal interpolation for CERES flux products, *J.*
898 *Atmos. Ocean. Tech.* (submitted).
899
900 Draper, N. and H. Smith (1981), Applied Regression Analysis, Second Edition. *Wiley*, ISBN
901 047102995-5.
902
903 Fasullo, J. T., and K. E. Trenberth (2008), The annual cycle of the energy budget. Part II: Meridional
904 structures and poleward transports, *J. Clim.*, *21*, 2313-2325.
905
906 Folland, C. K., J. A. Renwick, M. J. Salinger, and A. B. Mullan (2002), Relative influences of the
907 Interdecadal Pacific Oscillation and ENSO on the South Pacific Convergence Zone, *Geophys. Res.*
908 *Lett*., *29*, 13 doi:10.1029/2001GL014201.
909
910 Gruber, A., R. Ellingson, P. Ardanuy, M. Weiss, S. K. Yang, and S. N. Oh (1994), A comparison of
911 ERBE and AVHRR longwave flux estimates, *Bull. Am. Meteorol. Soc.*, *75*, 2115-2130.
912
913 Iacono, M. J., J. S. Delamere, E. J. Mlawere, M. W. Shephard, S. A. Clough, and W. D. Collins
914 (2008), Radiative forcing by long-lived greenhouse gases: Calculations with the AER radiative
915 transfer models, *J. Geophys. Res*., *113*, D13103, doi:10.1029/2008JD009944.
916

917 Jones, C., L. M. V. Carvalho, R. W. Higgins, D. E. Waliser, and J. K. E. Schemm (2004),
918 Climatology of tropical intraseasonal convective anomalies: 1979-2002, *J. Clim.*, *17*, 523-539.
919
920 Kidson, J. W., M. J. Revell, B. Bhaskaran, A. B. Mullan, and J. A. Renwick (2002), Convection
921 patterns in the Tropical Pacific and their influence on the atmospheric circulation at higher latitudes,
922 *J. Clim.*, *15*, 137-159.
923
924 Kiladis, G. N., K. H. Straub, and P. T. Haertel (2005), Zonal and vertical structure of the Madden-
925 Julian Oscillation, *J. Atmos. Sci.*, *62*, 2790-2809.
926
927 Kyle, H. L., A. Arking, J. R. Hickey, P. E. Ardanuy, H. Jacobowitz, H. Jacobowitz, L. L. Stowe, G.
928 G. Campbell, T. Vonder Haar, F. B. House, R. Maschhoff, and G. L. Smith (1993), The Nimbus
929 Earth Radiation Budget (ERB) Experiment: 1975-1992, *Bull. Am. Meteorol*. *Soc*., *74*, 815-830.
930
931 Loeb, N. G., S. Kato, K. Loukachine, and N. Manalo-Smith (2005), Angular distribution models for
932 top-of-atmosphere radiative flux estimation from the Clouds and the Earth's Radiant Energy System
933 instrument on the *Terra* satellite. Part 1: Methodology, *J. Atmos. Ocean. Tech*., *22*(4), 338-
934 351.doi:10.1175/JTECH1712.1.
935
936 Loeb, N. G., S. Kato, W. Su, T. Wong, F. Rose, D. Doelling, J. Norris (2012a), Advances in
937 understanding top-of-atmosphere radiation variability from satellite observations, *Surveys in*
938 *Geophysics*, doi:10.1007/S10712-012-9175-1.
939

940 Loeb, N. G., J. M. Lyman, G. C. Johnson, R. P. Allan, D. R. Doelling (2012b), Observed changes in
941 top-of-the-atmosphere radiation and upper-ocean heating consistent within uncertainty, *Nature*
942 *Geoscience*, doi:10.1038/NGE01375 and supplementary information.
943
944 McClatchey, R. A., R. W. Fenn, J. E. A. Selby, F. E. Volz, and J. S. Garing (1972), Optical
945 Properties of the Atmosphere (Third Edition), *Environ. Res. Papers*, *411*, AFCRL, Bedford, MA, 108
946 pp.
947
948 Mehta, A. V. and J. Susskind (1999a), Outgoing Longwave Radiation from the TOVS Pathfinder
949 Path A data set, *J. Geophys. Res*., *104*, 12193-12212.
950
951 Mehta, A. V. and J. Susskind (1999b), Longwave Radiative Flux calculations in the TOVS
952 Pathfinder Path A data set. *NASA Tech. Rep., GSFC/CR-1999-208643*.
953
954 Minnis, P., Q. Z. Trepte, S. Sun-Mack, Y. Chen, D. R. Doelling, et al. (2008), Cloud detection in
955 non-polar regions for CERES using TRMM VIRS and Terra and Aqua MODIS data, *IEEE Trans.*
956 *Geosci. Remote Sens*., *46*, 3857-3884.
957
958 Minnis, P., S. Sun-Mack, D. F. Young, P. W. Heck, D. P. Garber, et al. (2011), CERES Edition-2
959 cloud property retrievals using TRMM VIRS and Terra and Aqua MODIS data. Part 1: Algorithms,
960 *IEEE Trans. Geosci. Remote Sens*., *49*, doi:10.1109/TGRS.2011.2144601.
961
962 Power, S. B., and I. N. Smith (2007), Weakening of the Walker Circulation and apparent dominance
963 of El Niño both reach record levels, but has ENSO really changed?, *Geophys. Res. Lett*., *34*, L18702,
964 doi:10.1029/2007GL030854.

965

966 Soden, B. J., and I. M. Held (2006), An assessment of climate feedbacks in coupled ocean–
967 atmosphere models, *J. Clim.*, *19*, 3354-3360.

968

969 Soden, B. J., I. M. Held, R. Colman, K. M. Shell, J. F. Kiehl, C. A. Shields (2008), Quantifying
970 climate feedbacks using radiative kernels, *J Clim.*, *21*, 3504-3520.

971

972 Susskind, J. and J. E. Searl (1978), Synthetic atmospheric transmittance spectra near 15 μm and 4.3
973 μm, *J. Quant. Spectr. Rad. Trans*., *19*, 195-215.

974

975 Susskind, J., P. Piraino, L. Rokke, L. Iredell, and A. V. Mehta (1997), Characteristics of the TOVS
976 Pathfinder Path A data set, *Bull. Am. Meteorol. Soc*., *78*, 1449-1472.

977

978 Susskind, J., C. D. Barnet, J. M. Blaisdell (2003), Retrieval of atmospheric and surface parameters
979 from AIRS/AMSU/HSB data in the presence of clouds, *IEEE Trans. Geosci. Remote Sens.*, *41*, doi:
980 10.1109/TGRS.2002.808236, 390-409.

981

982 Susskind, J., J. Blaisdell, and L. Iredell (2009), Improved determination of surface and atmospheric
983 temperatures using only shortwave AIRS channels, *Proc. SPIE International Symp. Infrared*
984 *Spaceborne Remote Sensing and Instrumentation XVII*, San Diego, CA.

985

986 Susskind, J., J. M. Blaisdell, L. Iredell, and F. Keita (2011), Improved temperature sounding and
987 quality control methodology using AIRS/AMSU data: The AIRS Science Team Version 5 retrieval
988 algorithm. *IEEE Trans. Geosci. Remote Sens.*, *99*, 1-25, doi:10.1109/TGRS.2010.2070508.

989

990 Susskind, J., J. Blaisdell, and L. Iredell (2012), Significant advances in the AIRS Science Team
991 Version-6 retrieval algorithm, *Proc. SPIE International Symp. Infrared Spaceborne Remote Sensing*
992 *and Instrumentation XX*, Paper #8510-29, San Diego, CA.
993
994 Trenberth, E. T., J. T. Fasullo, C. O'Dell, and T. Wong (2010), Relationships between tropical sea
995 surface temperature and top-of-atmosphere radiation, *Geophys. Res. Lett*., *37*, L03702,
996 doi:10.1029/2009GL042314.
997
998 Vonder Haar, T. H., J. L. Bytheway, and J. M. Forsythe (2012), Weather and climate analyses using
999 improved global water vapor observations, Geophys. Res. Lett., *39*, L15802,
1000 doi:10.1029/2012GL052094.
1001
1002 Wielicki, B. A., B. R. Barkstrom, E. F. Harrison, R. B. Lee III, G. L. Smith, and J. E. Cooper (1996),
1003 Clouds and the Earth's Radiant Energy System (CERES): An Earth Observing System experiment,
1004 *Bull. Am. Meteor. Soc*., *77*, 853-868.
1005
1006 Wong, T., B. A. Wielicki, R. B. Lee, III, G. L. Smith, K. A. Bush, J. K. Willis (2006),
1007 Reexamination of the observed decadal variability of the Earth Radiation Budget using altitude-
1008 corrected ERBE/ERBS nonscanner WFOV data, *J. Clim.*, *19*, 4028-4040.
1009
1010 Zelinka, M. D., and D. L. Hartmann (2011), The observed sensitivity of high clouds to mean surface
1011 temperature anomalies in the tropics, *J. Geophys. Res*., *116*, D23103, doi:10.1029/2011JD016459.
1012

1013 Zelinka, M. D., S. A. Klein, and D. L. Hartmann (2012a), Computing and partitioning cloud
1014 feedbacks using cloud property histograms. Part 1: Cloud radiative kernels, *J. Clim.*, 25, 3715-3735.
1015
1016 Zelinka, M. D., S. A. Klein, and D. L. Hartmann (2012b), Computing and partitioning cloud
1017 feedbacks using cloud property histograms. Part 2: Attribution to the nature of cloud changes, *J.*
1018 *Clim.*, 25, 3736-3754.
1019
1020 Zhou, Y. P., K.-M. Xu, Y. C. Sud, and A. K. Betts (2011), Recent trends of the tropical hydrological
1021 cycle inferred from Global Precipitation Climatology Project and International Satellite Cloud
1022 Climatology Project data, *J. Geophys. Res*., 116, D09101, doi: 10.1029/2010JD015197.
1023
1024
1025
1026
1027
1028
1029
1030
1031
1032
1033
1034
1035
1036

Table 1a. OLR Anomaly Time Series Comparison
September 2002 through June 2011

Data Set	Global	Tropical
AIRS ARC ($W/m^2/yr$)	−0.094 ± 0.026	−0.183 ± 0.070
CERES Terra ARC ($W/m^2/yr$)	−0.059 ± 0.022	−0.154 ± 0.066
AIRS Minus CERES STD (W/m^2)	0.136	0.155
AIRS/CERES Correlation	0.955	0.991

Global and tropical mean statistical comparisons of AIRS and CERES OLR anomaly time series for the period September 2002 through June 2011. Shown are the Average Rates of Change, the standard deviations between the anomaly time series, and the temporal correlations of the anomaly time series.

Table 1b. OLR_{CLR} Anomaly Time Series Comparison
September 2002 through June 2011

Data Set	Global	Tropical
AIRS ARC ($W/m^2/yr$)	−0.021 ± 0.020	−0.072 ± 0.042
CERES Terra ARC ($W/m^2/yr$)	−0.089 ± 0.020	−0.144 ± 0.044
AIRS Minus CERES STD (W/m^2)	0.222	0.247
AIRS/CERES Correlation	0.772	0.936

Global and tropical mean statistical comparisons of AIRS and CERES OLR_{CLR} anomaly time series for the period September 2002 through June 2011. Shown are the Average Rates of Change, the standard deviations between the anomaly time series, and the temporal correlations of the anomaly time series.

Table 1c. Correlations between Global and Tropical Mean OLR and OLR_{CLR} Anomaly Time Series, September 2002 through June 2011

AIRS and CERES

	Global OLR	Tropical OLR	Global OLR_{CLR}	Tropical OLR_{CLR}	Niño-4 Index
Global OLR	**---**	**0.705**	**0.720**	**0.608**	**0.587**
Tropical OLR	0.646	**---**	**0.616**	**0.871**	**0.830**
Global OLR_{CLR}	0.797	0.696	**---**	**0.799**	**0.502**
Tropical OLR_{CLR}	0.663	0.928	0.827	**---**	**0.730**
Niño-4 Index	0.523	0.813	0.618	0.808	**---**

Temporal correlations of AIRS and CERES OLR and OLR_{CLR} global and tropical mean anomaly time series. Correlations using AIRS data records are shown above the diagonal in bold and those using CERES data are shown beneath the diagonal.

Table 2. Area Mean Statistics for AIRS and CERES OLR
September 2002 through June 2011

	AIRS		CERES	
Spatial Area	OLR ARC ($W/m^2/yr$)	OLR ENC	OLR ARC ($W/m^2/yr$)	OLR ENC
WPMC Region	-1.502 ± 0.525	0.871	-1.496 ± 0.529	0.870
Tropical outside WPMC Region	0.004 ± 0.054	0.050	0.034 ± 0.053	0.101
Global outside WPMC Region	-0.030 ± 0.028	-0.129	0.005 ± 0.027	-0.372
EEPA Region	-0.631 ± 0.158	0.767	-0.611 ± 0.154	0.761
Tropical outside EEPA Region	-0.037 ± 0.048	0.599	-0.011 ± 0.047	0.511
Global outside EEPA Region	-0.044 ± 0.020	0.256	-0.011 ± 0.019	0.039

Area mean Average Rates of Change of AIRS and CERES OLR anomaly time series, and the correlation between the OLR anomaly time series and the El Niño Index, computed over different spatial domains for the period September 2002 through June 2011.

Figure and Table Captions

Figure 1

a) Monthly mean global mean time series values of AIRS Version-5 and CERES Terra Edition-2.6 OLR and OLR_{CLR} for the period September 2002 through June 2011. Monthly mean values of AIRS Version-6 OLR and OLR_{CLR} products are also shown for ten months for which they have been calculated. b) Global monthly mean differences of values shown for Figure 1a. The green and red horizontal lines show the average values of the differences between AIRS and CERES OLR and AIRS and CERES OLR_{CLR}, respectively.

Figure 2

Monthly mean global mean AIRS and CERES OLR anomaly time series, and their differences for the period September 2002 through June 2011. a) Global mean OLR anomalies, b) Tropical mean (20°N to 20°S) anomalies, as well as the El Niño Index multiplied by 1.5, c) As in a) but for $OLR_{CLR,}$ d) As in b) but for OLR_{CLR}.

Figure 3

Spatial 1˚ latitude by 1˚ longitude distribution of OLR ARCs over the time period September 2002 through June 2011. The NOAA Niño-4 region is outlined in gray and the WPMC and EEPA regions are outlined in black in this and most subsequent figures showing spatial distributions of ARCs of different parameters. a) AIRS OLR ARCs, b) CERES OLR ARCs, c) AIRS OLR ARCs minus CERES OLR ARCs, d) AIRS Version-5 OLR ARCs minus AIRS Version-6 OLR ARCs.

Figure 4

Spatial 1˚ latitude by 1˚ longitude distribution of OLR correlations over the time period September 2002 through June 2011: a) AIRS OLR ENCs, b) CERES OLR ENCs, c) AIRS OLR ENCs minus CERES OLR ENCs, d) AIRS and CERES OLR temporal anomaly correlations.

Figure 5

Hovmöller diagram for time series of monthly mean anomalies (vertical scale) integrated over the latitude range 5˚N through 5˚S in each 1˚ longitude bin (horizontal scale) for the period September 2002 through June 2011. a) AIRS OLR, b) CERES OLR, c) the difference between AIRS OLR and CERES OLR anomalies.

Figure 6

Spatial distribution of ARCs and ENCs of AIRS retrieved geophysical parameters for the period September 2002 through June 2011. a) ARCs of Surface Skin Temperature (K/yr), b) ENCs of Surface Skin Temperature, c) ENCs of q_{500}, d) ENCs of $\alpha\varepsilon$.

Figure 7

Hovmöller diagrams of anomalies of AIRS retrieved products. The longitudinal domain of the NOAA Niño-4 region is encompassed by the gray vertical lines. a) $T_{skin}(K)$, b) $q_{500}(\%)$, c) $\alpha\varepsilon(\%)$.

Figure 8

A scatter plot comparing AIRS values of OLR ARC minus CERES OLR ARC (ΔOLR ARC) with those of cloud fraction ARC for all grid points 60°N to 60°S.

Table 1a

Global and tropical mean statistical comparisons of AIRS and CERES OLR anomaly time series for the period September 2002 through June 2011. Shown are the Average Rates of Change, the standard deviations between the anomaly time series, and the temporal correlations of the anomaly time series.

Table 1b

Global and tropical mean statistical comparisons of AIRS and CERES OLR_{CLR} anomaly time series for the period September 2002 through June 2011. Shown are the Average Rates of Change, the standard deviations between the anomaly time series, and the temporal correlations of the anomaly time series.

Table 1c

Temporal correlations of AIRS and CERES OLR and OLR_{CLR} global and tropical mean anomaly time series. Correlations using AIRS data records are shown above the diagonal in bold and those using CERES data are shown beneath the diagonal.

Table 2

Area mean Average Rates of Change of AIRS and CERES OLR anomaly time series, and the correlation between the OLR anomaly time series and the El Niño Index, computed over different spatial domains for the period September 2002 through June 2011.

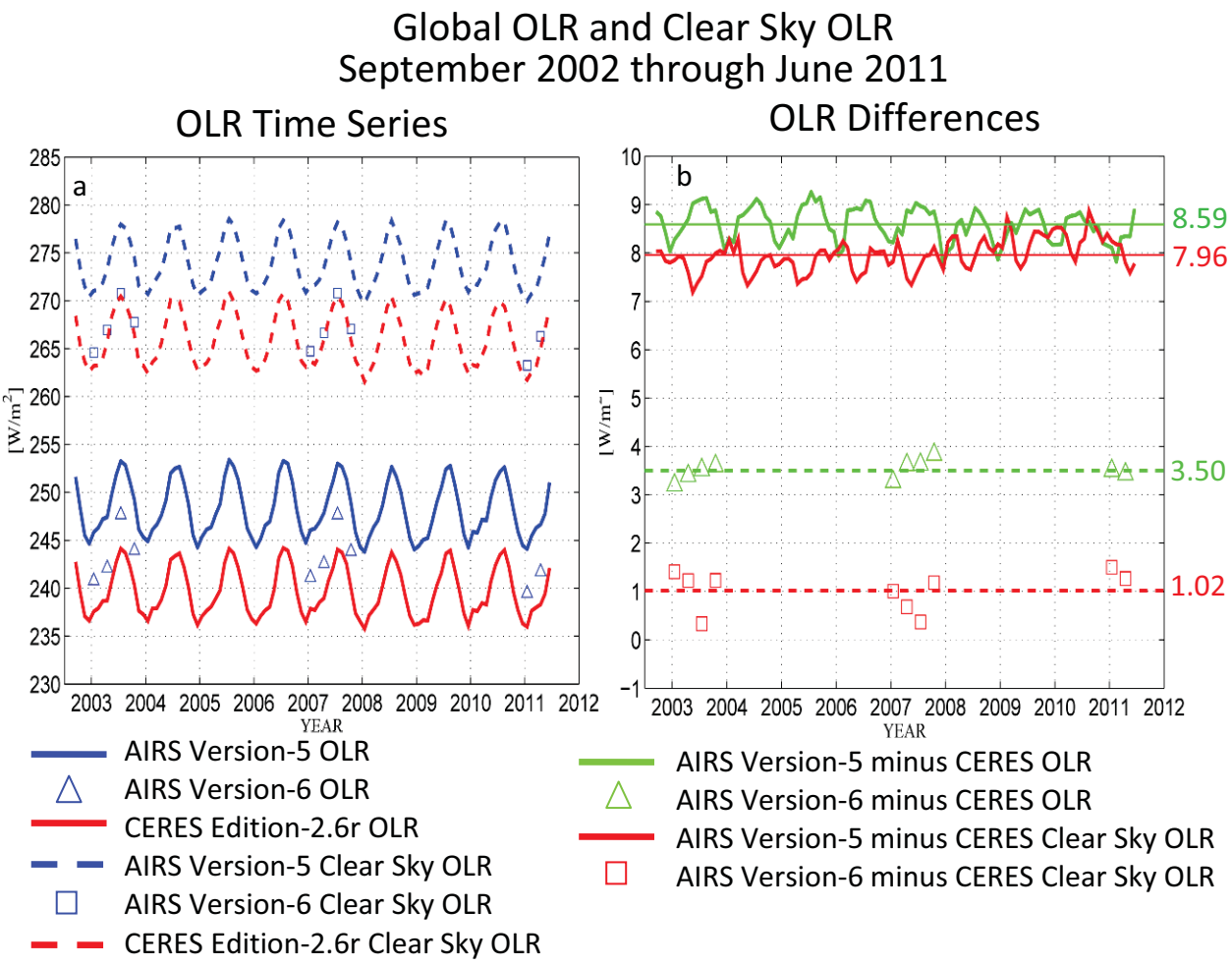
Global OLR and Clear Sky OLR
September 2002 through June 2011
OLR Time Series
OLR Differences
a
b
[W/m^2]
YEAR
8.59
7.96
3.50
1.02
AIRS Version-5 OLR
AIRS Version-6 OLR
CERES Edition-2.6r OLR
AIRS Version-5 Clear Sky OLR
AIRS Version-6 Clear Sky OLR
CERES Edition-2.6r Clear Sky OLR
AIRS Version-5 minus CERES OLR
AIRS Version-6 minus CERES OLR
AIRS Version-5 minus CERES Clear Sky OLR
AIRS Version-6 minus CERES Clear Sky OLR

Figure 1

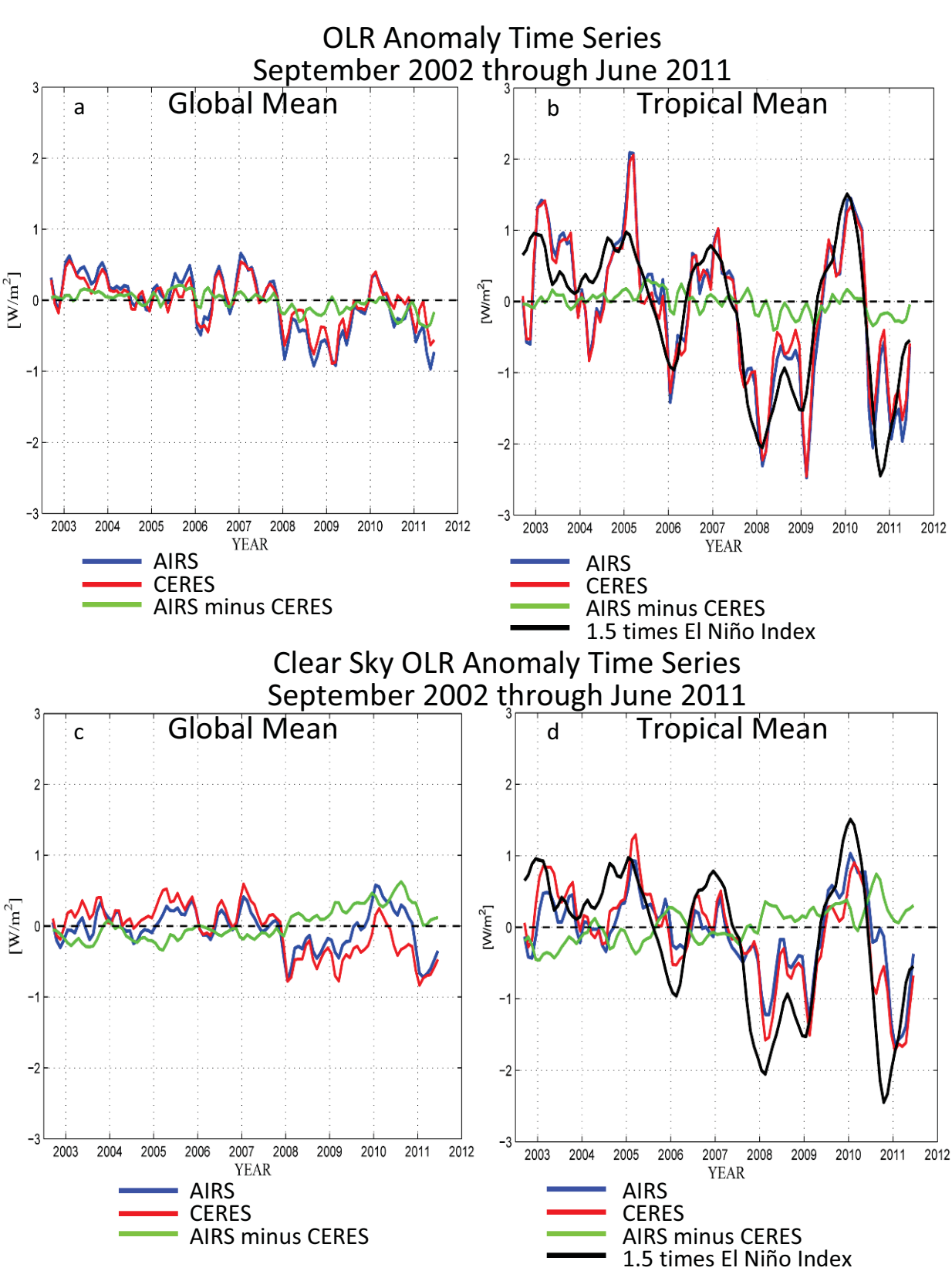
OLR Anomaly Time Series
September 2002 through June 2011
a
Global Mean
b
Tropical Mean
[W/m^2]
YEAR
AIRS
CERES
AIRS minus CERES
1.5 times El Niño Index
Clear Sky OLR Anomaly Time Series
September 2002 through June 2011
c
Global Mean
d
Tropical Mean

Figure 2

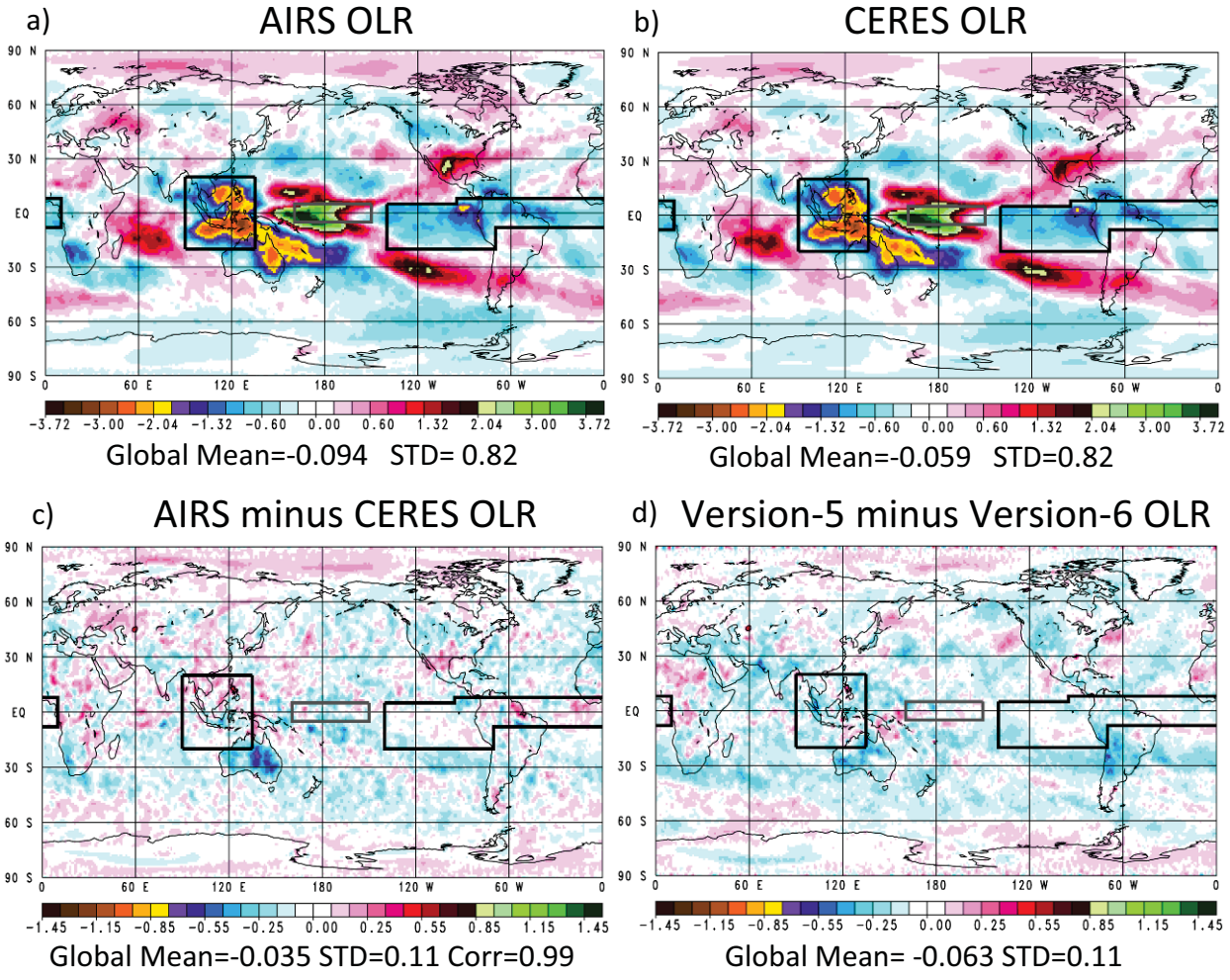
Average Rates of Change (W/m^2/yr)
September 2002 through June 2011
a) AIRS OLR
b) CERES OLR
Global Mean=-0.094 STD= 0.82
Global Mean=-0.059 STD=0.82
c) AIRS minus CERES OLR
d) Version-5 minus Version-6 OLR
Global Mean=-0.035 STD=0.11 Corr=0.99
Global Mean= -0.063 STD=0.11

Figure 3

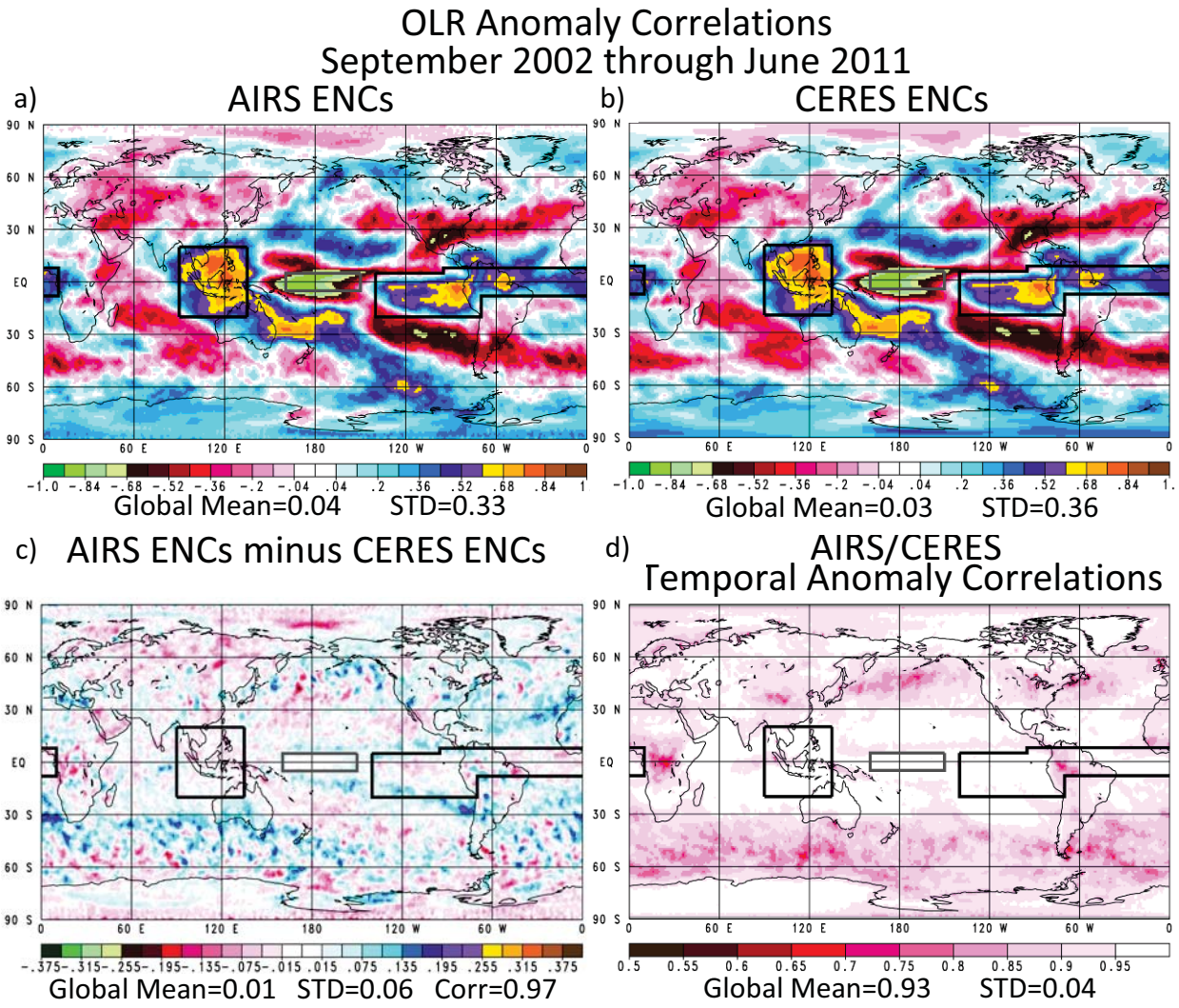
OLR Anomaly Correlations
September 2002 through June 2011
a) AIRS ENCs
b) CERES ENCs
Global Mean=0.04 STD=0.33
Global Mean=0.03 STD=0.36
c) AIRS ENCs minus CERES ENCs
d) AIRS/CERES
Temporal Anomaly Correlations
Global Mean=0.01 STD=0.06 Corr=0.97
Global Mean=0.93 STD=0.04

Figure 4

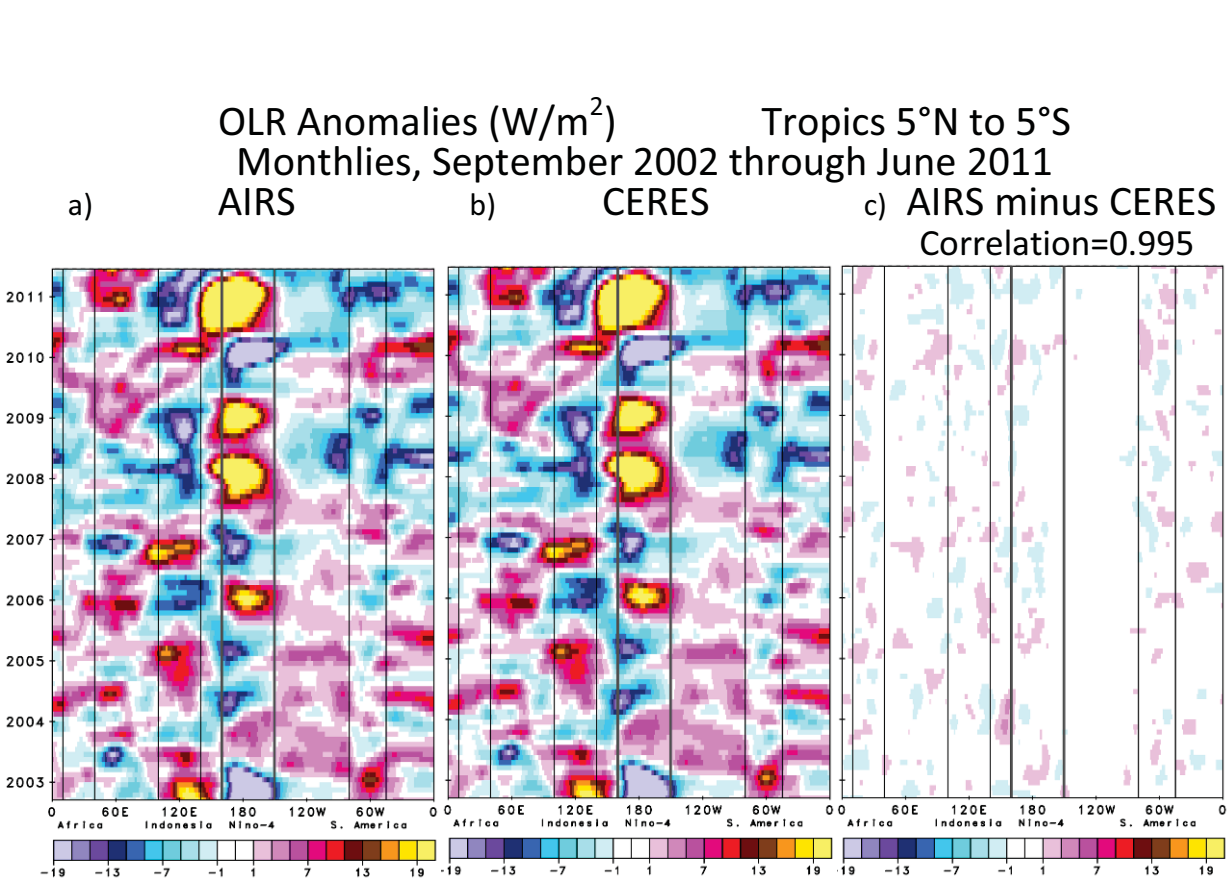
OLR Anomalies (W/m2)
Tropics 5°N to 5°S
Monthlies, September 2002 through June 2011
a) AIRS
b) CERES
c) AIRS minus CERES
Correlation=0.995
2011
2010
2009
2008
2007
2006
2005
2004
2003
0
60E
120E
180
120W
60W
Africa
Indonesia
Nino-4
S. America
-19
-13
-7
-1
1
7
13
19

Figure 5

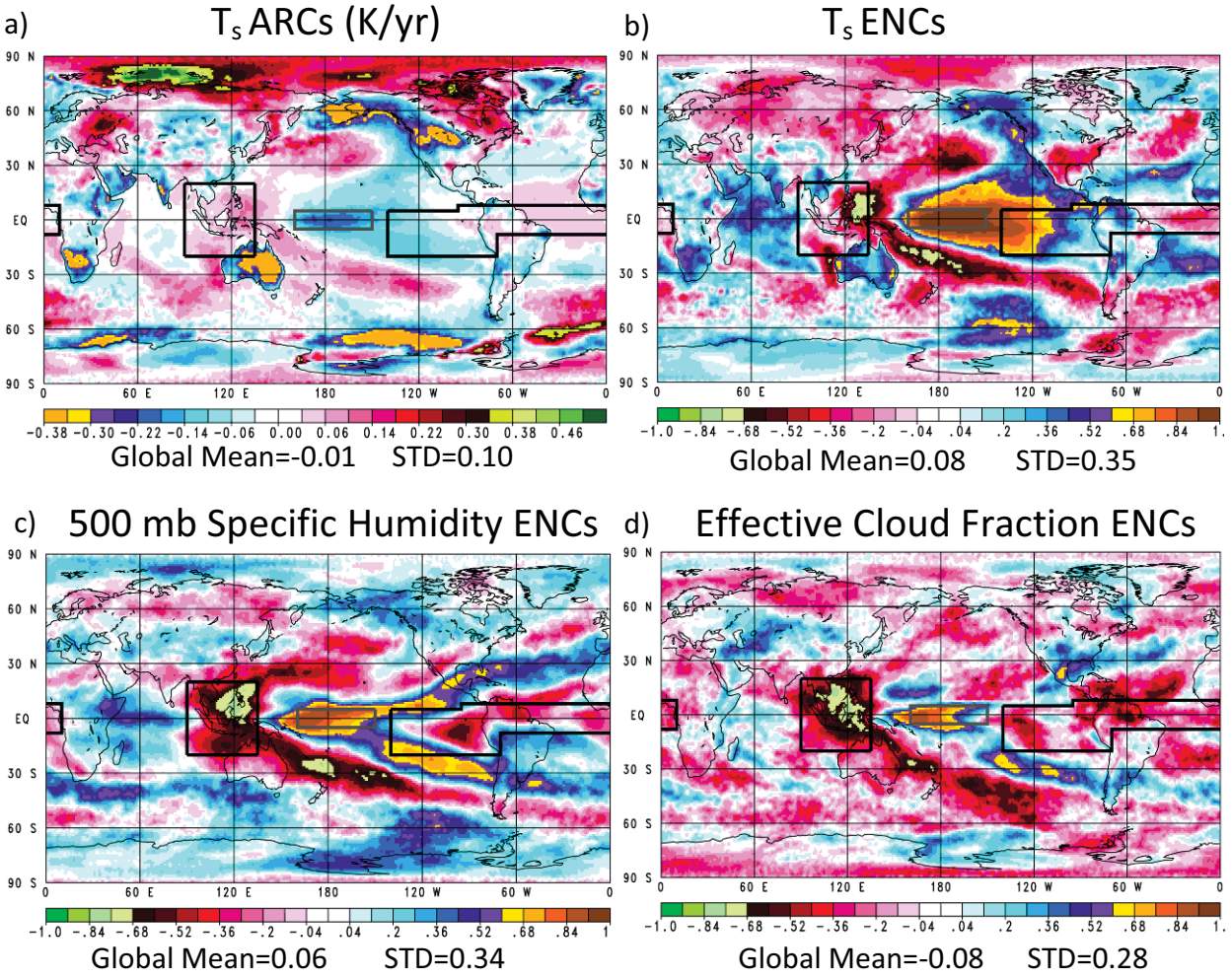
AIRS Products September 2002 through June 2011
a)
T_s ARCs (K/yr)
b)
T_s ENCs
Global Mean=-0.01 STD=0.10
Global Mean=0.08 STD=0.35
c)
500 mb Specific Humidity ENCs
d)
Effective Cloud Fraction ENCs
Global Mean=0.06 STD=0.34
Global Mean=-0.08 STD=0.28

Figure 6

AIRS Anomalies Tropics 5°N to 5°S
Monthlies, September 2002 through June 2011

a) Skin Temperature (K) b) 500 mb Specific Humidity (%) c) Cloud Fraction (%)

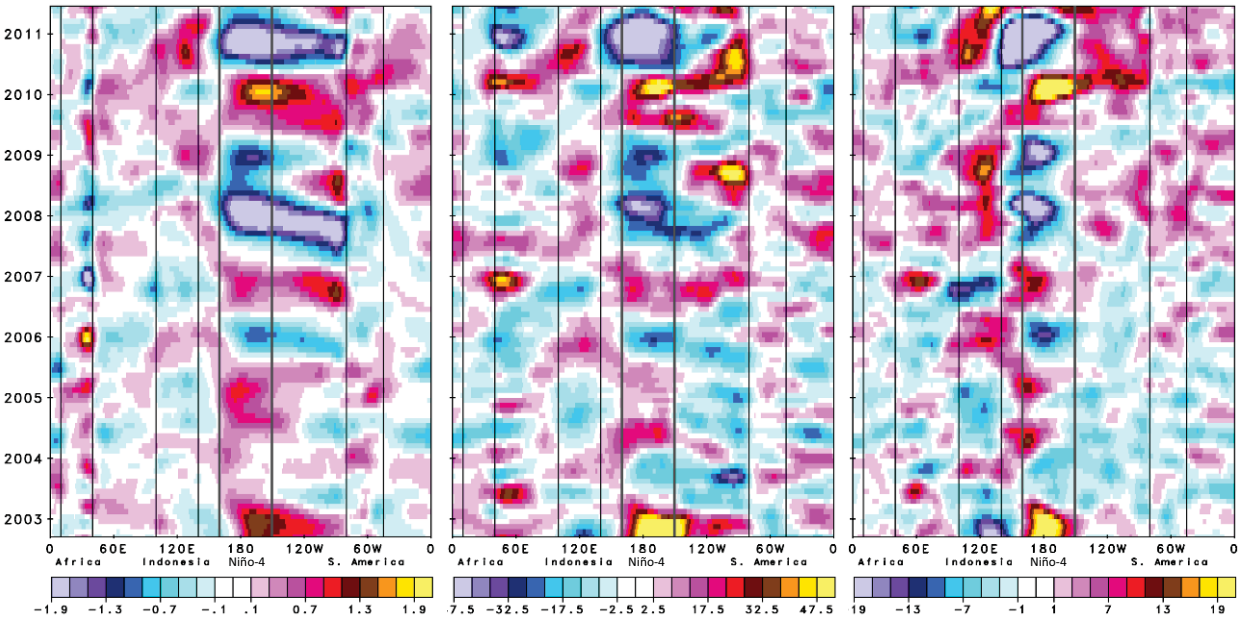

Figure 7

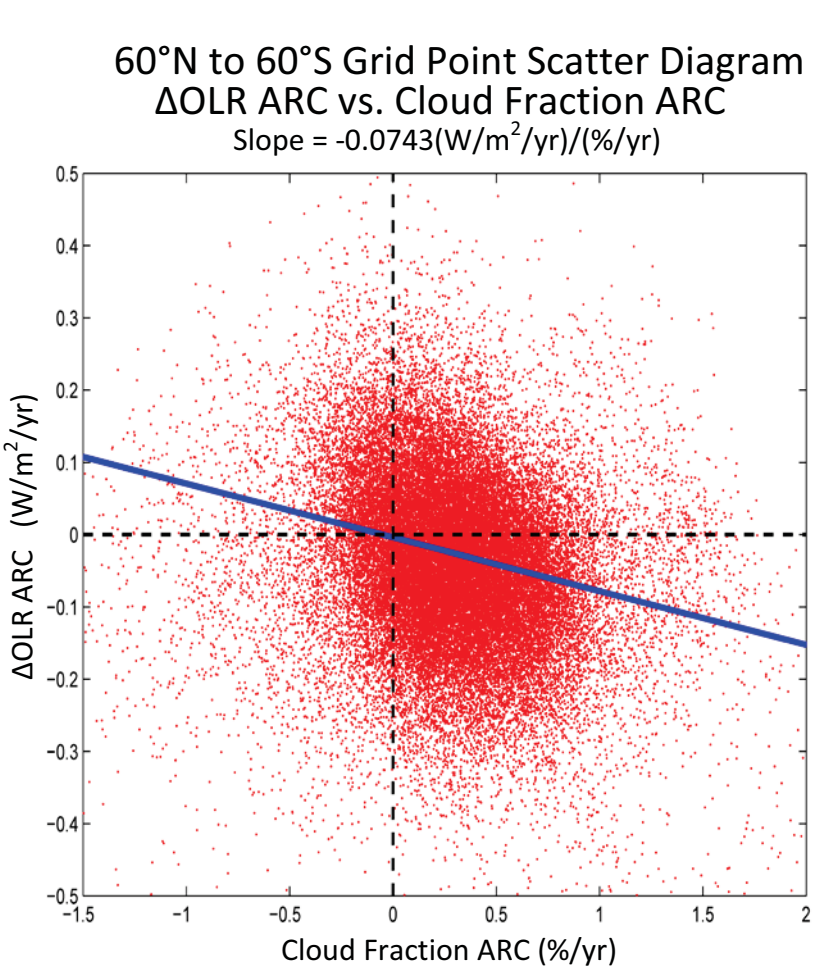
60°N to 60°S Grid Point Scatter Diagram
ΔOLR ARC vs. Cloud Fraction ARC
Slope = -0.0743(W/m2/yr)/(%/yr)
ΔOLR ARC (W/m2/yr)
Cloud Fraction ARC (%/yr)
0.5
0.4
0.3
0.2
0.1
0
-0.1
-0.2
-0.3
-0.4
-0.5
-1.5
-1
-0.5
0
0.5
1
1.5
2

Figure 8